energies

MDPI

Article

First-Principles Study of the Structural Stability and Dynamic Properties of Li_2MSiO_4 (M = Mn, Co, Ni) Polymorphs

Ponniah Vajeeston *, Federico Bianchini and Helmer Fjellvåg

Center for Materials Sciences and Nanotechnology, Department of Chemistry, University of Oslo, P.O. Box 1033 Blindern, N-0315 Oslo, Norway; federico.bianchini@smn.uio.no (F.B.); helmer.fjellvag@kjemi.uio.no (H.F.)

* Correspondence: ponniahv@kjemi.uio.no; Tel.: +47-22855613

Received: 29 November 2018; Accepted: 7 January 2019; Published: 11 January 2019

Abstract: In recent years, the scientific community has shown an increasing interest in regards to the investigation of novel materials for the intercalation of lithium atoms, suitable for application as cathodes in the new generations of Li-ion batteries. Within this framework, we have computed the relative structural stability, the electronic structure, the elastic and dynamic properties of Li_2MSiO_4 compounds (M = Mn, Co, Ni) by means of first-principles calculations based on density functional theory. The so-obtained structural parameters of the examined phases are in agreement with previous reports. The energy differences between different polymorphs are found to be small, and most of these structures are dynamically stable. The band structures and density of states are computed to analyse the electronic properties and characterise the chemical bonding. The single crystal elastic constants are calculated for all the examined modifications, proving their mechanical stability. These Li_2MSiO_4 materials are found to present a ductile behaviour upon deformation. The diffusion coefficients of Li ions, calculated at room temperature for all the examined modifications, reveal a poor conductivity for this class of materials.

Keywords: cathode materials; Li ion battery; structural stability; mechanical stability; DFT study; relative stability; electronic structure; transport properties

1. Introduction

Lithium-ion batteries present an excellent combination of high energy and power density and consequently are currently the most promising technology for energy storage devices as well as for electric vehicles [1,2]. In the course of the last 20 years, this technology has established as the dominant one for rechargeable battery for portable devices. However, their application in other areas is more challenging due to the demanding requirements of high power capability at low cost for large systems and the need of improving the overall safety [3]. The development of novel Li-ion batteries is thus attracting the interest of the scientific community, aimed at the design and production of a high-energy, low-cost and long-life battery technology. The cathode materials are the bottleneck of this Li-ion technology in terms of both the cost of raw materials and the theoretical capacity. Researching novel materials exhibiting a high specific capacity and good retention of the latter upon electrochemical cycling, as well as high operating voltage is therefore crucial in order to advance the overall state of the art of Li-ion-based battery technology. In this context, the main advantage of polyoxyanion intercalation compounds with respect to transition metal oxides is the greater stability upon intercalation/deintercalation of Li^+ ions, ensured by the covalence of the bonding between oxygen and the non-metallic atom (e.g., P, Si). This feature ensures an improved capacity retention,

as well as better overall battery safety. Phosphate materials, particularly $LiFePO_4$, have been the object of detailed studies and have been proven to be excellent cathode materials. While phosphates continue to be relevant, the interest of a large community has recently shifted towards silicates, such as Li_2FeSiO_4, due to the natural abundance of these elements and their consequently low cost. Li_2MSiO_4 (M = Mn, Fe, Co, Ni) is one of the promising cathode materials for lithium ion batteries, not only because it presents stable polyanion structures, but also due to the larger theoretical capacity with respect to existing cathode materials, due to the possibility of two-electron redox processes [4–8].

Li_2MnSiO_4 has more advantages than Li_2FeSiO_4 with regards to cell safety, ease of preparation and cost effectiveness. The $Mn^{3+} \leftrightarrow Mn^{4+}$ conversion provides a higher potential than Mn^{2+}/Mn^{3+} and Fe^{2+}/Fe^{3+} (it is yet to be clarified whether this involves an Fe^{3+}/Fe^{4+} redox couple or it might just be an electrolyte degradation phenomenon [9–12]). In practical applications, Li_2MnSiO_4 is limited as a cathode by its low electronic conductivity of $\sim 5 \times 10^{-16}$ S cm^{-1} at room temperature (RT) (and $\sim 3 \times 10^{-14}$ S cm^{-1} at 60 °C), which is 5–6 orders of magnitude smaller than that of $LiFePO_4$ at RT. Co- or Ni-containing salts for preparing Li_2CoSiO_4 and Li_2NiSiO_4 are commercially expensive and environmentally toxic. Li_2NiSiO_4, with the lowest band-gap, does not have the shortcomings of Mn derivatives [9], but the delithiation potentials (>4.6 V) of Li_2CoSiO_4 and Li_2NiSiO_4 are too high to make the present electrolytes suitable Li^+ diffusion media. To explore the suitability of silicate materials as sustainable cathode materials for rechargeable Li ion batteries, the voltage plateaus [13–16], cycling and structural stabilities [14,17–20], electrical and ionic conductivities [20–22], site-exchange [23], effect of mixed transition metal [9,24], addition of Na [25,26], high-pressure behavior [18,27] of Li_2MSiO_4 (M = Fe, Mn, Co and Ni) were investigated by several first principles calculations studies.

Li_2MSiO_4 compounds belong to a family of tetrahedral oxide structures that consist of slightly distorted close-packed oxygen layers. The cations occupy half of the tetrahedral sites and several distinct ordering patterns are possible, It has been shown that both the crystal structure and the polarisation of a Li_2MSiO_4 cathode are substantially modified during the first few cycles. The voltage and the kinetics change accordingly. Eventually, a more stable structure is obtained, at the expense of the capacity of the cathode [16]. Half of the Li, M, and Si atoms rearrange upon cycling, resulting in significantly different Li^+ diffusion pathways. The suitability of Li_2MSiO_4 for application as cathode materials was discussed in a work dating back 1997, following the early success of the phosphate electrode [28] The electrochemistry of Li_2FeSiO_4, Li_2FeGeO_4 and L_2MnSiO_4 towards Li^+/Li has been investigated, revealing average operating voltages of ca. 3.1 V, 3.05 V and 4.2 V, respectively. Yang and coworkers succeeded in removing for the first time both lithium atoms from Li_2MnSiO_4 [9]. The electrode is shown to suffer a large polarization as a result of the complete delithiation.

More recently, a great deal of work has been dedicated to addressing the shortcomings of these materials, including capacity fading and low ionic conductivity. The beneficial calcium doping in the Li_2MnSiO_4 matrix has been extensively studied in [29]. A Ca^{2+} ion, shown to preferably occupy the Mn site, is shown to act as a pillar ion, helping to maintain the structural integrity if Li_2MnSiO_4 and to reduce the Li/Mn disorder of the pristine material, leading to an improved ionic conductivity. On top of that, calcium doping is also shown to lower the binding energy of Mn, thus facilitating the extraction of the second Li^+ ion, resulting in a larger capacity. In [30], the electrochemical performance of a carbon-coated Li_2MnSiO_4 cathode is shown to be enhanced by fluorine doping. The ionic conductivity is greatly improved, due to the double effect of: (i) increasing the equilibrium volume and (ii) reducing the C-O bonding in the carbon layers. Fluorine doping is also shown to increase the structural stability of the cathode and decrease average particle sizes. In [31] the collaborative effect of carbon-coating and P doping is investigated for a Li_2CoSiO_4 cathode. The carbon-coated sample is a stable mixture of $Pmn2_1$ and $Pbn2_1$ particles, with improved capacity retention with respect to the pristine material. P-doping is shown to suppress the formation of $Pbn2_1$ and to increase the experimental capacity of the cathode by promoting the two-lithium intercalation mechanism. A similar effect is reported in reference [32] for Al doping of a carbon-coated Li_2CoSiO_4 cathode.

In a previous work, we have reported the structural stability, dynamical and mechanical properties of the Li_2FeSiO_4 system [18]. We extend here our study to the physical properties of the Li_2MSiO_4 (M = Mn, Co, Ni), providing in particular a detailed characterisation of the structural stability, electronic structure, and Li-transport properties of the Li_2MSiO_4 systems.

2. Materials and Methods

Density functional theory calculations were performed using the Vienna *ab initio* simulation package with projected-augmented wave (PAW) potentials [33,34]. The exchange and correlation functionals are treated within the general gradient approximation (GGA), following the approach of Perdew, Burke, and Ernzerhof (PBE) [35]. The Hubbard parameter U is introduced following the rotationally invariant form [36,37]. Effective U values of 4 eV and 4.1 eV were used for the Mn-d, Co-*d* and Ni-*d* states, respectively.

The optimised geometries were obtained by iterative minimisation of the Hellman-Feynman forces and stress tensor, by means of the conjugate-gradient algorithm with force tolerance of 10^{-3} eV Å^{-1}. Integration over the Brillouin zone was performed using a Monkhosrt-Pack grid and a Gaussian broadening of 0.1 eV. From various sets of calculations it was determined that 512 **k** points ($8 \times 8 \times 8$ grid) and a 600 eV plane-wave cutoff are sufficient to ensure optimum accuracy in the computed results. From the previously reported total-energy calculation for the Li_2FeSiO_4-$Pmn2_1$ phase we have found that the antiferromagnetic (AFM) and ferromagnetic (FM) states are lower in energy compared to the paramagnetic (PM) state [18]. The energy difference between AFM and FM states is 2 meV/cell, to the close to the accuracy threshold of our calculations, and both configurations exhibit a similar volume of the elementary cell. Hence, in the present work we have considered only the FM states for all the examined phases (i.e., all the M atoms are treated as up spin configuration with the finite magnetic moment (5 μB)).

The total energy has been calculated as a function of the cell volume and fitted to the universal equation of state (EOS) [38]. The transition pressures are then obtained from the Gibbs free energy ($G = U + PV - TS$ where T = 0; G = total energy + pressure × volume), calculated following the procedure presented in [39]. A frozen phonon calculation was performed using suitable supercells models, using the phonopy software to calculate the phonon dispersion and the associated density of states [40]. A displacement of 0.0075 Å was applied to the atoms, with a symmetry considerations, to obtain the force constants matrix. Displacements along opposite directions were included to improve the accuracy. The dynamical matrices were calculated from the force constants, and phonon density of states (PhDOS) curves were computed on a Monkhorst-Pack grid [41]. The thermal properties, including heat capacity, free energy and entropy, were obtained from the calculated PhDOS.

The barrier height for the diffusion of a Li^+ ion calculated using the Nudged Elastic Band (NEB) on suitable supercell models ensuring that the atoms are separated from their periodic image and thus providing a more accurate result. The dimensions of these systems is reported in Table S1. To determine the minimum energy path (MEP) through the NEB method [42,43], five replicas of the system were created by linear interpolation between the initial and final states.

3. Result and Discussions

3.1. Structure Models Considered

In general, a good agreement is found between experimental data and theoretical DFT-based predictions using structural inputs from the Inorganic Crystal Structure Database (ICSD) [44]. In the course of our long experience in modelling and predicting the structural properties of hydrides and oxides (see [45–47]), we have found that the ICSD/guess approach is a very robust method for identifying local minima and predicting phase transitions, provided that a sufficiently large set of existing configurations is provided. We have analysed input structures from 486 entries with ABC_2X_4 composition. Note that the effective set of configuration used is much smaller, as several

compounds/phases share the same structure type and, in some cases, only small variations in the positional parameters are present for certain atoms. Even though we used different positional parameters, these structures often relaxed to the similar type of structural arrangement upon geometry optimization and hence these possibilities are omitted. By the end of this screening process, we end uo with 11 distinct structure types with ABC_2X_4 formulae. These structure types are (space group and space group number in the parenthesis; illustrated in Figure 1): Li_2FeSiO_4 ($P2_1$; 4), Li_2BeSiO_4 (Pn; 7), Li_2FeSiO_4 ($P2_1/n$; 14), Li_2BeSiO_4 ($C222_1$; 20), Li_2FeSiO_4 ($Pmn2_1$; 31), Li_2CoSiO_4 ($Pna2_1$; 33), Li_2FeSiO_4 ($Pnma$; 62), Li_2CaSiO_4 (I-$42m$; 121), $EuLi_2SiO_4$ ($P3_12_1$; 152), Li_2BaSiO_4 ($P6_3cm$; 185), and Li_2MnSiO_4-modified-$Pmn2_1$ (here after its called as $Pmn2_1$-mod structure). The cycled $Pmn2_1$ structure is named as $Pmn2_1$-mod structure. The $Pmn2_1$-mod structure can be described as the site-exchange of half of the Li ions and all of the Fe ions in the pristine Li_2FeSiO_4 structure (in the pristine $P2_1/n$ structure, the Li^+ and Fe^{2+} occupy different crystallographic sites, whereas in the cycled structure, the sites normally occupied by Fe^{2+} are now occupied exclusively by Li^+, while the remaining Li^+ and Fe ions share the conventional Li sites). The structure of cycled Li_2FeSiO_4 can be understood as a 3D framework connected by [SiO_4] and [FeO_4] tetrahedra, with Li ions occupying the interstitial tetrahedral sites.

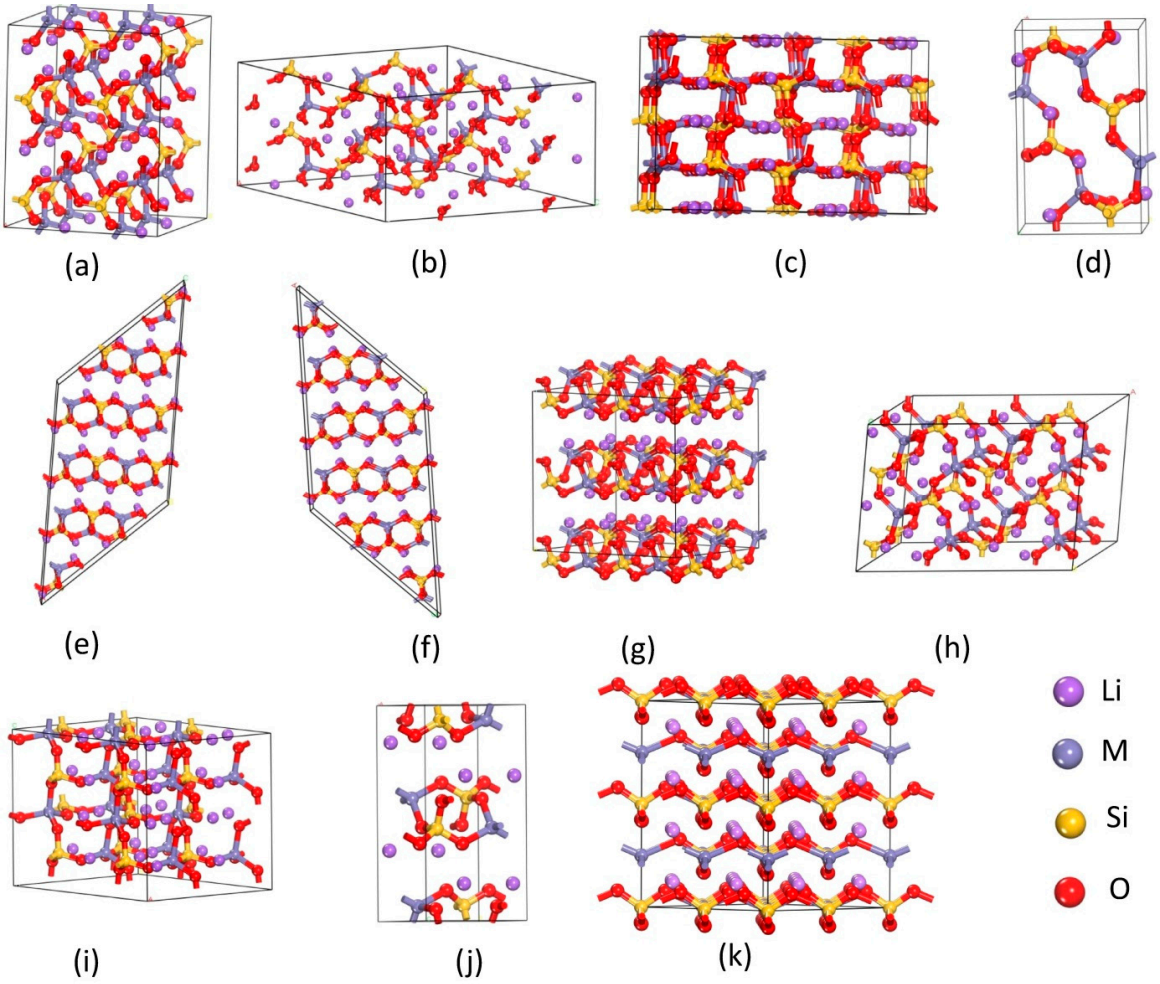

Figure 1. Considered structure models for the present theoretical simulations: (**a**) Li_2BeSiO_4 ($C222_1$); (**b**) Li_2BeSiO_4 (Pn); (**c**) $P2_1/n$-*n-cycled*; (**d**) Li_2CoSiO_4 ($Pna2_1$) (**e**) Li_2FeSiO_4 ($P2_1/n$); (**f**) Li_2FeSiO_4 ($P2_1$); (**g**) Li_2FeSiO_4 ($Pmn2_1$); (**h**) *modified-*$Pmn2_1$; (**i**) $Pmn2_1$-*ncycled* and (**j**) Li_2FeSiO_4 ($Pmna$); (**k**) Li_2CaSiO_4 ($I222$). The legends for the different kinds of atoms are given in the illustration.

At ambient condition most of the Li_2MSiO_4 compounds stabilised in orthorhombic ($Pmn2_1$) structure synthesis by various synthesis methods (like hydrothermal methods [48,49], solid-state [5,50], solgel [12,51], spray pyrolysis [52], microwave [53] and combustion methods [54], etc.). It is very stable compound and easy to synthesize *via* all these techniques.

3.1.1. Li_2MnSiO_4

There are four known Li_2MnSiO_4 polymorphs that form at ambient pressure. Two orthorhombic (i.e., $Pmn2_1$ and $Pmnb$) and two monoclinic ($P2_1/n$ and Pn) modifications. Politaev et al. synthesised monoclinic ($P2_1/n$) Li_2MnSiO_4 at 950–1050 °C *via* a solid-state method [55]. The monoclinic Pn phase transforms into an orthorhombic phase ($Pmn2_1$) at temperatures above 370 °C [56]. A second, reversible phase transition can be observed by rate-cooling. The orthorhombic ($Pmnb$) modification, synthesied at 800 °C using a solid-state method, transformed to the a $P2_1/n$ phase when cooled to RT at 200 K min^{-1}. The synthesis performed at 700 °C, on the other hand, produced the $Pmn2_1$ phase thus indicating that the $Pmnb$ phase transformed into orthorhombic disordered structures analogue to wurtzite [57]. The low-temperature orthorhombic modifications are more stable than the monoclinic form, because of their larger volume. The latter can only be produced using high temperature (above 900 °C) synthesis [58]. Experimental investigations clearly reveal that by increasing the s pressure or the temperature of the process, the structural transformations ($Pmn2_1 \rightarrow Pmnb \rightarrow P2_1/n$) will take place [27,58].

Among the structures considered for structural optimization, the $Pmn2_1$ atomic arrangement is found to exhibit the lowest total energy (see Figure 2). The calculated atomic sites and lattice parameters (see Tables 1 and 2) are in good agreement with experimental findings [5] and with other theoretical calculations [58]. In this structure, chains of LiO_4 tetrahedra run along the ***a*** direction, parallel to the chains of alternating MnO_4 and SiO_4 tetrahedra. The second most energetically favourable phase is orthorhombic $Pbn2_1$. The energy difference between these two phases at the equilibrium volume is only ca. 30 meV/f.u. (see Figure 2) [59,60]. Interestingly, the energy difference between the $Pmn2_1$-mod., Pc, $P2_1/n$, and $Pmnb$ is also very small, and hence, one can easily modify one polymorph into another by application of temperature or pressure; this explains the difficulties in controlling the synthesis of single phase Li_2MnSiO_4 samples, also related to very similar electrochemical properties (voltage, volume variation upon delithiation, and electronic structure) [27,58].

Table 1. The calculated equilibrium structural parameters (*a*, *b* and *c* are in Å), bandgap (E_g in eV), bulk modulus (in GPa) and its derivative for Li_2MSiO_4 polymorphs.

Phase	Lattice Parameter				E_g (eV)	*Bo*	*Bo′*
	a	*b*	c	*β(deg)*			
Li_2MnSiO_4-$P2_1/n$	6.4102 (6.3360) [a]	10.9932 (10.9146) [a]	5.1034 (5.0730) [a]	91.1 (90.99) [a]	2.94	47	3.8
Li_2MnSiO_4-$Pbn2_1$	6.3382	10.9504	5.0512	90	2.90	46	3.8
Li_2MnSiO_4-$Pmn2_1$	6.3250 (6.3109) [b]	5.3842 (5.3454) [b]	5.0031 (4.9624) [b]	90	2.97	47	4.0
Li_2MnSiO_4-$I222$	4.4033	4.4033	6.4288	90	1.56	58	4.1
Li_2CoSiO_4-$Pbn2_1$	6.2782 (6.253) [c]	10.084 (10.685) [c]	5.282 (4.929) [c]	90	2.39	44	3.9
Li_2CoSiO_4-Pn	8.2320 (8.231) [b]	5.0168 (5.022) [b]	8.2348 (8.232) [b]	99.18 (99.27)	3.15	42	4.0
Li_2CoSiO_4-$I222$	4.2823	4.2823	6.6211	90	2.2	58	3.7
Li_2NiSiO_4-$P2_1$	8.4536	5.0858	8.4682	100.25	2.35	43	4.0
Li_2NiSiO_4-$Pmn2_1$	6.3210 (6.294) [d]	5.4755 (5.3702) [d]	5.1002 (4.9137) [d]	90	1.3	42	4
Li_2NiSiO_4-$I222$	4.4203	4.4203	6.9204	90	1.72	56	3.6
Li_2NiSiO_4-$P2_1$	8.4536	5.0858	8.4682	100.25	2.35	43	4.0

[a] From ref. [55]; [b] From ref. [5]; [c] From ref. [61]; [d] From ref. [9].

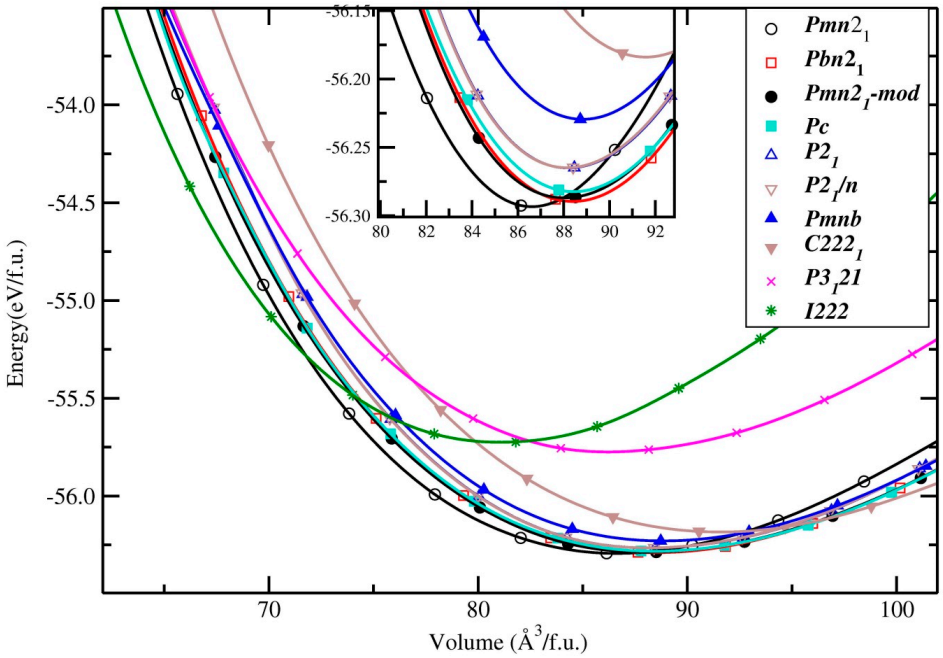

Figure 2. Calculated unit cell volume vs. total energy (per formula unit; f.u.) for Li_2MnSiO_4 in actual and possible structural arrangements (structure types being labeled on the illustration). For a better visualisation of data, we have displayed only the results for the 10 most favourable structures. The magnified version in proximity of the minima of the curves is shown as an insert.

Table 2. Theoretically calculated (derived from the total energies) equilibrium lattice parameters (a, b and c in Å) for Li_2MSiO_4 polymorphs.

Compound	Space Group	Positional Parameters
Li_2MnSiO_4	$Pmn2_1$	Li (4b): 0.7490, 0.3281, 0.9420; Mn (2a): $\frac{1}{2}$, 0.175, 0.4384; Si (2a): 0, 0.1766, 0.4502; O1 (4b): 0.71224, 0.6813, 0.8404; O2 (2a): $\frac{1}{2}$, 0.1175, 0.8496; O3 (2a): $\frac{1}{2}$, 0.8205, 0.2820
	$Pbn2_1$	Li (4a): −0.1607, 0.0034, 0.2580; Li (4a): −0.4233, 0.7444, 0.2582; Mn (4a): −0.1660, 0.4965, 0.2589; Si (4a): −0.4141, 0.2524, 0.2640; O1 (4a): −0.4122, 0.2544, 0.5911; O2 (4a): −0.5566, 0.2520, 0.1557; O2 (4a): −0.3312, 0.0360, 0.1641; O2 (4a): −0.3445, 0.4668, 0.1528
	*I*222	Li (4d): −1/2, 0, $\frac{1}{4}$; Mn (2b): −1/2, $\frac{1}{2}$, 0; Si (2a): 0, 0, 0; O (8i): −0.2132, 0.2133, 0.1288
Li_2CoSiO_4	$Pbn2_1$	Li (4a): −0.1596, −0.0012, 0.2548; Li (4a): −0.4255, 0.750, 0.2541; Co (4a): −0.1697, 0.4864, 0.2545; Si (4a): −0.4129, 0.2418, 0.2646; O1 (4a): −0.4090, 0.2357, 0.5960; O2 (4a): −0.5547, 0.2418, 0.1641; O2 (4a): −0.3392, 0.0319, 0.1503; O2 (4a): −0.3473, 0.64625, 0.1641
	Pn	Li (2a): −0.5, 0.1602, −0.9993; Li (2a): 0.2469, 0.3262, −0.4990; Ni (2a): -0.2437, 0.3332, −0.4951 Si (2a): 0.9877, 0.1662, −0.0099; O1 (2a): −0.3438, 1719, −0.3454; O3 (2a): 0.0879, 0.1233, −0.4081; O3 (2a): −0.1232, 0.6891, −0.4081; O4 (2a): −0.6863, 0.3080, −0.8978
	*I*222	Li (4d): 0, $\frac{1}{2}$,$\frac{1}{4}$; Co (2b): 0, 0, $\frac{1}{2}$; Si (2a): 0, 0, 0; O1(8i): 0.2784, 0.2784, 0.6304
Li_2NiSiO_4	$P2_1$	Li (2a): 0.6593, 0.9166, 0.6623; Li (2a): 0.1598, 0.8134, 0.1621; Li (2a): 0.5818, 0.4112, 0.0884; Li (2a): 0.0815, 0.383, 0.5883; Ni (2a): 0.2879, 0.9167, 0.5358; Ni (2a): 0.7886, 0.8136, 0.0363; Si (2a): 0.0444, 0.8106, 0.7953; Si (2a): 0.5449, 0.9200, 0.2955; O1 (2a): 0.8656, 0.9064, 0.8318; O2 (2a): 0.3659, 0.8241, 0.3316; O3 (2a): 0.4258, 0.3121, 0.8823; O4 (2a): 0.9263, 0.4183, 0.3824; O5 (2a): 0.6875, 0.8084, 0.4409; O6 (2a): 0.1873, 0.9218, 0.9408; O7 (2a): 0.9514, 0.9829, 0.2049; O8 (2a): 0.4505, 0.7475, 0.7047
	$Pmn2_1$	Li (4b): 0.751, 0.3256, 0.9385; Ni (2a): $\frac{1}{2}$, 0.1818, 0.4359; Si (2a): 0, 0.16204, 0.4497; O1 (4b): 0.7119, 0.6922, 0. 8502; O2 (2a): $\frac{1}{2}$, 0.1275, 0.8372; O3 (2a): $\frac{1}{2}$, 0.8439, 0.2851
	*I*222	Li (4d): 0, $\frac{1}{2}$, $\frac{1}{4}$; Co (2b): 0, 0, $\frac{1}{2}$; Si (2a): 0, 0, 0; O1 (8i): 0.2709, 0.2709, 0.6270

In order to determine the critical pressure of these structural transitions we have displayed in Figure 3 the Gibbs free-energy of the involved crystallographic structures, using the low energy structure as a reference for every pressure value. As discussed above, $Pmn2_1$ is the more favourable structure, and it transforms into the *I*222 modification at 8.2 GPa (see Figure 3). The *I*222 structure is

closely related to the *I*-42*m* (space group 121). These modifications are found to have the same energy within standard DFT accuracy.

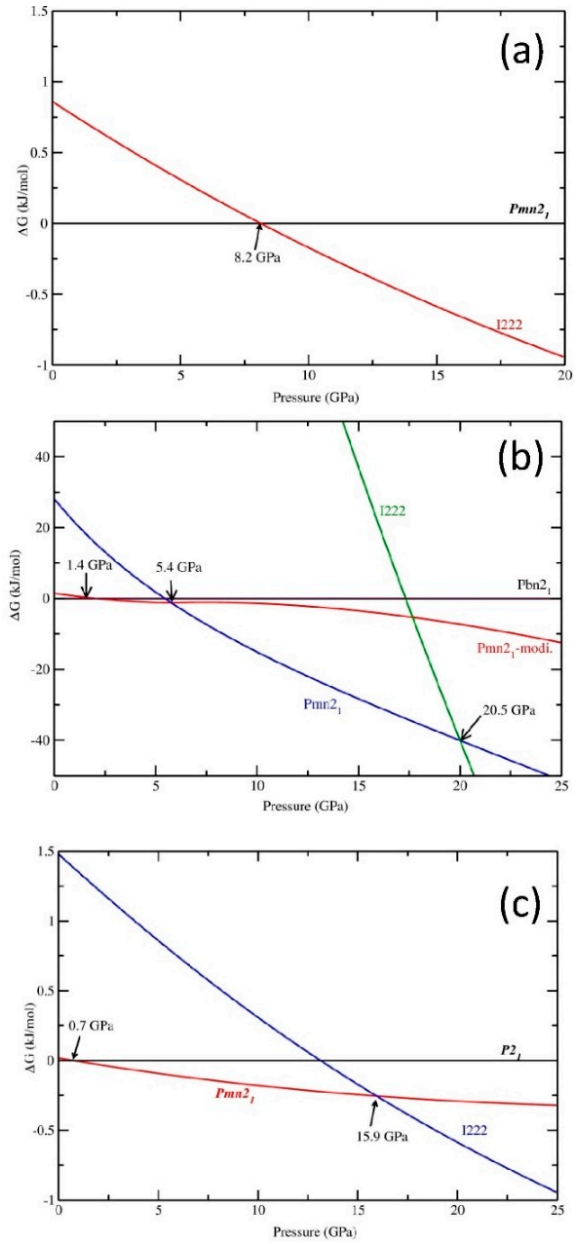

Figure 3. Calculated stability diagram (difference in Gibbs free energy ΔG) for (**a**) Li_2MnSiO_4 related to *Pmn*2$_1$ phase; (**b**) Li_2CoSiO_4 related to *Pbn*2$_1$ phase and (**c**) Li_2NiSiO_4 related to *P*2$_1$ phase. Transition points are marked by arrows with the corresponding transition pressure.

3.1.2. Li_2CoSiO_4

Like Li_2MnSiO_4, Li_2CoSiO_4 also crystallises in four different polymorphs [62–64] which can be formed by rapid cooling (0.5 °C min^{-1}) from above 1000 °C resulted in the formation of *Pmnb*, while slow cooling (0.1 °C min^{-1}) produced the *P*2$_1$/*n* phase. *Pmn*2$_1$ was formed by static heating of any other phase at 640–800 °C followed by quenching, and *Pbn*2$_1$ was formed by slow cooling of *Pmn*2$_1$ [56].

Monoclinic Li_2CoSiO_4 (*P*2$_1$/*n*) was prepared at 950 °C and transformed (at 900 °C) into the orthorhombic *Pmn*2$_1$ and *Pna*2$_1$ phases under 40/60 kbar, respectively. Both cell volumes are smaller than in the monoclinic case. [62] Orthorhombic Li_2CoSiO_4 (*Pmn*2$_1$) was synthesised hydrothermally

(150 °C/72 h). It transformed to the orthorhombic ($Pna2_1$) phase when heated at 700 °C over 2 h and to a monoclinic ($P2_1/n$) phase at 1100 °C over 2 h [65].

Theoretically simulated energy-volume curves for Li_2CoSiO_4 are displayed in Figure 4. According to our simulation at 0 K, Li_2CoSiO_4 crystalises in orthorhombic ($Pbn2_1$) and has lower energy than the other structures. This structure is based on a distorted hexagonal-close-packing arrangement of O atoms with layers stacked parallel to (001) [64]. The cations occupy half of the available tetrahedral sites and are distributed over the sites on one side of the O layers; three of the four O atoms forming a cation-oxygen tetrahedron (MO_4) are in an O layer, and all pyramids of the MO_4 tetrahedra have the same orientation with respect to the layer. The SiO_4 and LiO_4 tetrahedral pairs share corners to form a chain along ***a***, and these chains are held together through other corners, thus forming puckered layers parallel to (010). In the same way, the CoO_4 and LiO_4 tetrahedral pairs form a chain along ***a***, and these chains also form puckered layers parallel to (010). These two kinds of layers are held together through common corners, thus forming a three-dimensional framework. This structure is isotypic with the low-temperature form of Li_3PO_4 [66] and essentially the same as that of Li_2ZnSiO_4 [64]. It is interesting to note that, in addition to the $Pbn2_1$ phase, the *Pn* and *the* $Pmn2_1$-mod phases exhibit also very similar energies and equilibrium volumes. The involved energy difference between with respect to $Pbn2_1$ are 0.8 and 1.8 meV for *Pn and* $Pmn2_1$-mod, respectively. This proximity in energy clearly suggests that one can easily change the structure from one phase to another. Application of pressure on this $Pbn2_1$ modification transforms it into $Pmn2_1$-mod at 1.4 Gpa. Larger pressures would transform this phase into $Pmn2_1$ and then into the *I*222 structure. The involved pressure for the phase transition between the $Pbn2_1$–to–$Pmn2_1$-mod, $Pmn2_1$-mod–to–$Pmn2_1$, and $Pmn2_1$–to–*I*222 are 1.4, 5.4 and 20.2 GPa, respectively.

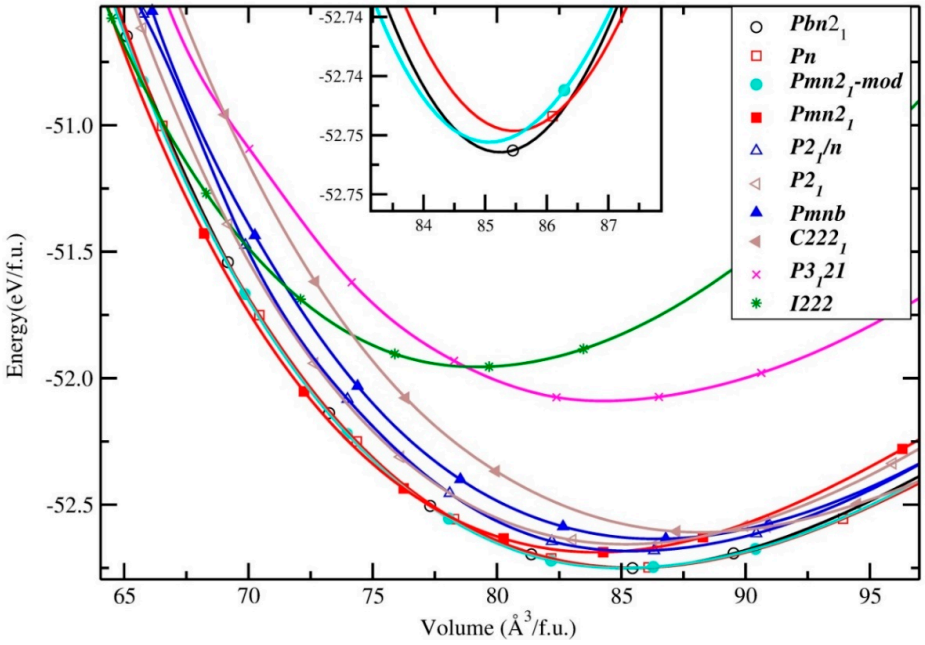

Figure 4. Calculated unit cell volume vs. total energy (per formula unit; f.u.) for Li_2CoSiO_4 in actual and possible structural arrangements (structure types being labeled on the illustration). The magnified version in proximity of the minima of the curves is shown as an insert.

3.1.3. Li_2NiSiO_4

Similar to the others two compounds described in this manuscript Li_2NiSiO_4 is also observed most frequently in its orthorhombic structure ($Pmn2_1$). DFT calculations predict that Li_2NiSiO_4 has very large deintercalation potentials (4.5 V for Ni^{2+}/Ni^{3+} and 5.2 V for Ni^{3+}/Ni^{4+}) [20,67], resulting in a challenging electro-chemical behaviour, even though the Li_2NiSiO_4 powder had been successfully

synthesized [9,20]. Among the three compounds studied in this work Li_2NiSiO_4 is not yet well studied experimentally. The calculated total energy vs. volume relations for these structures are shown in Figure 5. Among the 11 structure types considered here, the monoclinic $P2_1$ and $P2_1/n$ structures exhibit similar total energies (see Figure 5). The next energetically favorable structure is the experimentally observed $Pmn2_1$ modification. At the equilibrium volume, the energy difference between these three phases is indeed very small. The involved energy difference between the $P2_1$ and $Pmn2_1$ is only 12 meV (see Figure 5). This proximity in energy suggests that the formation of these phases will strongly depend on external temperature/pressure conditions. For the $Pmn2_1$ modification, the calculated structural parameters are also in very good agreement with the observations [9]. The calculated cell parameters differ by less than 1% from the experimental values. $P2_1$ is found to be the more favourable configuration and to transforms into the $Pmn2_1$–modification at 0.7 GPa. The application of an even larger pressure would produce the $I222$ modification at 15.9 GPa as shown in Figure 3.

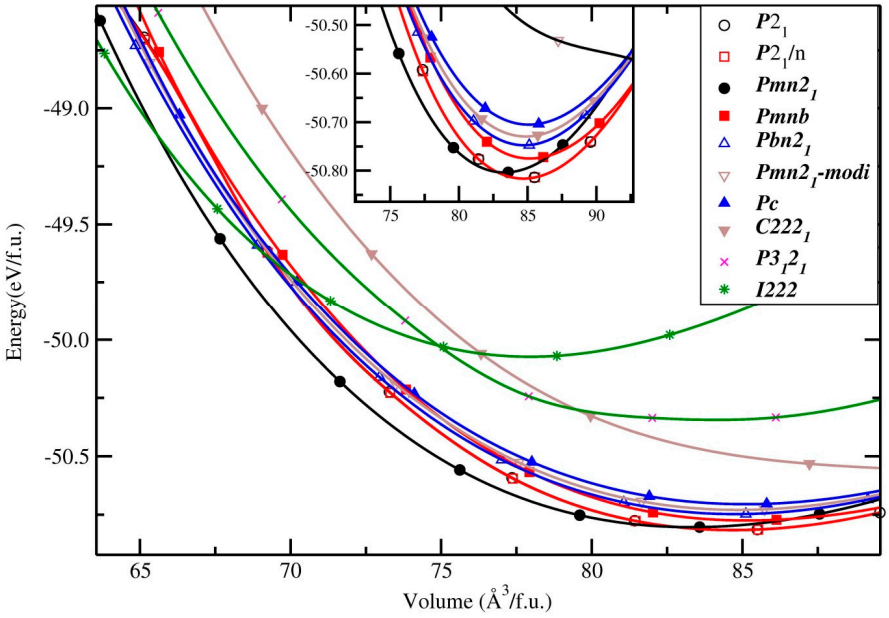

Figure 5. Calculated unit cell volume vs. total energy (per formula unit; f.u.) for Li_2NiSiO_4 in actual and possible structural arrangements (structure types being labelled on the illustration). The magnified version is proximity of the minima of the curves is shown as an insert.

3.2. Electronic Structure

In general, the poor electronic conductivity is known as a limiting factors for the application of silicates as electrodes [4–8]. In the present work, we calculate the total density of states (DOS) and its projection onto atomic orbitals (PDOS) for Li_2MSiO_4, with the aim of better understanding and potentially improving the electrical conductivity in these materials. Plots of these quantities are shown in Figure 6 (only for Li_2MnSiO_4 in $Pmn2_1$ is displayed and the remaining are shown in Figures S1–S4), and the calculated band gaps of Li_2MSiO_4 are reported in Table 3. Li_2MSiO_4 modifications exhibit large band gaps (>1.3 eV), and are consequently poor conductors of electrons. It is well known that the bandgap (E_g) values of solids obtained using standard DFT calculations are underestimated due to the discontinuity in the exchange-correlation potential. These values are commonly 30–50% smaller than the experimental references. Hence, the compounds under examination are likely to have a larger bandgap value than the one computed in this study. Among the Li silicates, the HP- Li_2MSiO_4 phases present the lower band gap width. These phases exhibit, however, the worst ionic conductivity in the series. The electronic conductivity is increased but the layer to layer interactions are decreases as a result the ionic conductivity decreases. The calculated total and site projected up and down spin

DOS of Li_2MnSiO_4 in $Pmn2_1$ phase is shown in Figure 7 where the vertical line indicates Fermi level (E_F). The DOS histogram of Li_2MSiO_4 consists of three parts: (a) the low-energy peak, mainly due to the localised semi-core *s* electrons of Si, (b) the bonding states of *M*-*d*, Si-*p*, O-*p*, and Li-*s* orbitals near the Fermi level; and (c) the top of the DOS curve due to antibonding states. It is found that the Si-s electrons are localized and naturally their contribution to the bonding is very small. The electrons from M-*d*, Si-*p* and the O-2*p* states both contribute to the density of states near to the Fermi level. The DOS of M-*d*, Si-*p* and the O-*p* are energetically degenerate from the bottom of the valence band to the Fermi level, indicating the possibility of covalent bonding between Si and O, M and O atoms in all these compounds. Due to the charge transfer from the Li site the contribution of the Li-s states are very small (see Figure 7).

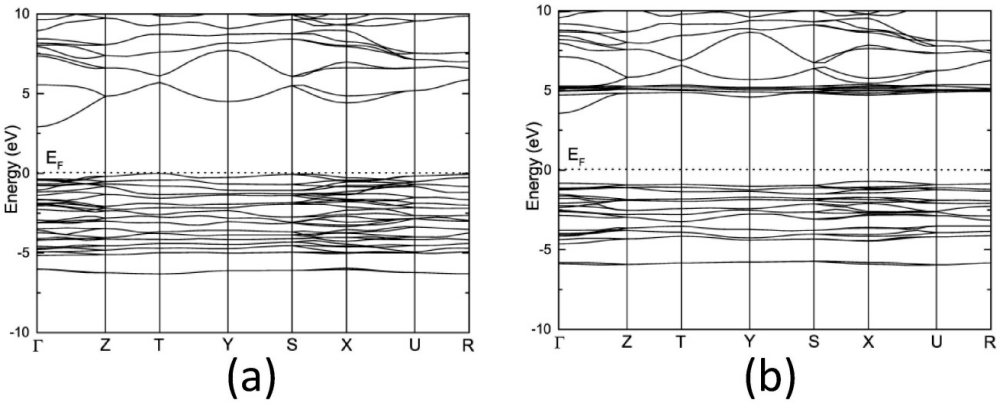

Figure 6. Calculated electronic up-spin (**a**) and down-spin (**b**) band structure of Li_2MnSiO_4 in $Pmn2_1$ structure. The Fermi level is set to zero.

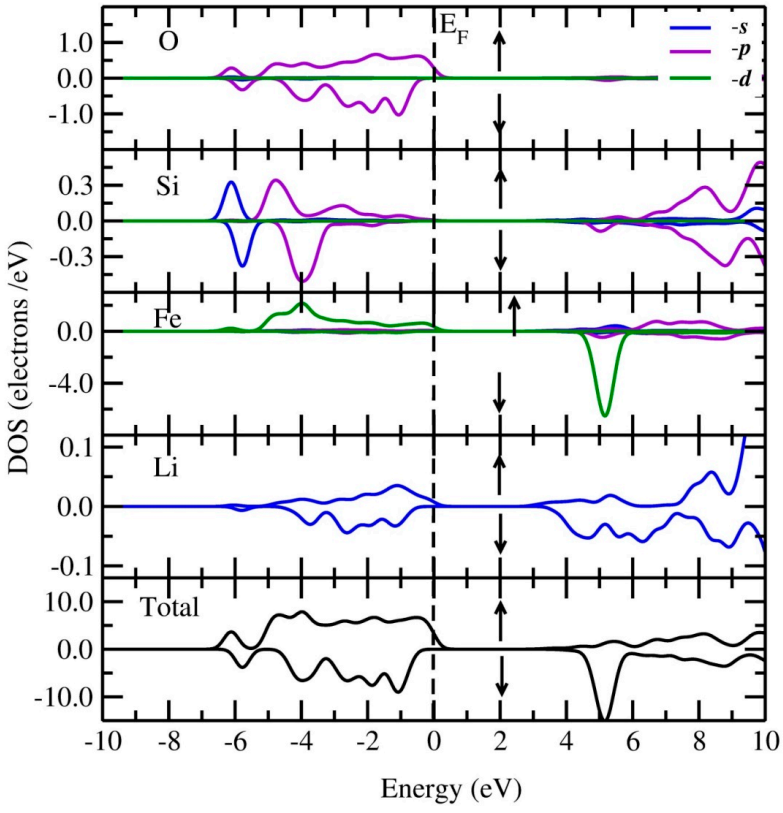

Figure 7. Calculated electronic up-spin and down-spin total DOS and site projected DOS of Li_2MnSiO_4 in $Pmn2_1$. The Fermi level is set to zero.

Table 3. The calculated single crystal elastic constants C_{ij} (in GPa), bulk modulus B (in GPa), shear modulus G (in GPa), Possion's ratio (σ), Young's modulus E (in GPa), compressibility (GPa^{-1}), Ductility, Lamè constant, longitudinal (v_L; in m/s), transverse (v_T; in m/s), and average sound velocity ($\acute{v}$ in m/s), and Debye temperature (Θ_D) for Li_2MSiO_4 polymorphs. Subscript V indicates the Voigt bound, R indicates the Reuss bound and VRH indicates the Hill average.

Properties	Phase								
	Li_2MnSiO_4			Li_2CoSiO_4			Li_2NiSiO_4		
	***Pmn*2$_1$**	***Pbn*2$_1$**	***I*222**	***Pbn*2$_1$**	***Pmn*2$_1$-*mod***	***I*222**	***P*2$_1$**	***Pmn*2$_1$**	***I*222**
C_{ij}	C_{11} = 192 C_{12} = 66 C_{13} = 70 C_{22} = 128 C_{23} = 42 C_{33} = 150 C_{44} = 47 C_{55} = 37 C_{66} = 49	C_{11} = 124 C_{12} = 65 C_{13} =55 C_{22} = 157 C_{23} = 60 C_{33} = 55 C_{44} = 37 C_{55} = 37 C_{66} = 43	C_{11} = 312 C_{12} = 165 C_{13} = 141 C_{22} = 320 C_{23} = 183 C_{33} = 270 C_{44} = 34 C_{55} = 59 C_{66} = 33	C_{11} = 119 C_{12} = 50 C_{13} = 40 C_{22} = 141 C_{23} = 38 C_{33} = 131 C_{44} = 47 C_{55} = 37 C_{66} = 44	C_{11} = 96 C_{12} = 36 C_{13} = 33 C_{15} = −16 C_{22} = 123 C_{23} = 29 C_{25} = 0 C_{33} = 115 C_{35} = 0 C_{44} = 417 C_{46} = 0 C_{55} = 34 C_{66} = 44	C_{11} = 336 C_{12} = 230 C_{13} = 199 C_{22} = 339 C_{23} = 249 C_{33} = 301 C_{44} = 9 C_{55} = 38 C_{66} = 13	C_{11} = 135 C_{12} = 38 C_{13} = 64 C_{15} = 0 C_{22} = 112 C_{23} = 43 C_{25}= 0 C_{33} = 157 C_{35} = 0 C_{44} = 46 C_{46} = 0 C_{55} = 42 C_{66} = 54	C_{11} = 203 C_{12} = 47 C_{13} = 50 C_{22} = 119 C_{23} = 36 C_{33} = 132 C_{44} = 47 C_{55} = 39 C_{66} = 45	C_{11} = 310 C_{12} = 214 C_{13} = 122 C_{22} = 378 C_{23} = 185 C_{33} = 229 C_{44} = 44 C_{55} = 52 C_{66} = 40
B_V	92	89	208	72	59		77	80	
B_R	86	88	181	72	59		71	75	
B_{VRH}	89	88	195	72	59		74	77	
G_V	46	40	53	43	40		46	48	
G_R	44	40	589	43	39		44	46	
G_{VRH}	45.5	40	321	43	39		45	47	
E	117	104	621	107	96		112	117	
Compressibility	0.01	0.01	0.005	0.01	0.01		0.01	0.01	
Ductility	0.5	0.5	1.64	0.6	0.7		0.6	0.609	
Lamè constant	59	61	−19	43	33		44	46	
σ	0.28	0.30	−0.03	0.25	0.23		0.25	0.247	
v_L	6973	6846	13709	6332	5889		6452	6527	
v_T	3844	3643	9841	3651	3499		3732	3784	
$\acute{v}$	4284	4070	10646	4053	3874		4142	4199	
Θ_D	1573	1485	4008	1498	1430		1532	1564	

3.3. Dynamical Stability

The total phonon density of states are calculated at the equilibrium volumes for different polymorphs of Li_2MnSiO_4 (shown in Figure 8). For the *I*222 modifications, the PhDOS are calculated at the phase transition point. The calculated PhDOS of Li_2MnSiO_4 polymorphs are displayed in Figure 8. Similarly, the total PhDOS of Li_2CoSiO_4 and Li_2NiSiO_4 are shown in Figure S5. For all the considered structures, imaginary frequencies were not observed (with the only exception of the *I*222 structure), indicating that all the structures dynamically stable at ambient conditions. The soft phonon modes observed for the *I*222 modification at the equilibrium volume disappear at pressures above 8.2 GPa for Li_2MnSiO_4 and 20.2, and 15.9 GPa for Li_2CoSiO_4 and Li_2NiSiO_4, respectively (see Figure 8 and Figure S4). Hence, these phases are predicted to be stable at the corresponding pressures (above the phase transition point). All the polymorphs of Li_2MnSiO_4, including the high-pressure phase, exhibit a similar phonon density of states. It is interesting to note that for the Li_2MnSiO_4 phase the energy difference between the *Pmn*2$_1$, *Pmn*2$_1$-mod., *Pc*, *P*2$_1$/*n*, and *Pmnb* phases are very small and, hence, one can easily modify one polymorph into another by application of temperature or pressure. Because of the similarity in the phonon spectra, we have displayed in Figure 9 only the partial phonon DOS for *Pmn*2$_1$ polymorphs. In the *Pmn*2$_1$ phase, the site projected phonon DOS is plotted in Figure 9 for Li, Fe, Si, and O atoms Figure 9. Because of the heavier mass of the Mn atom, the lower frequency modes in the phonon spectra are mainly originated from the Mn contribution. Due to their similar atomic arrangement, of the O atoms exhibit similar phonon density, even though they are located at different crystallographic sites, labelled O1, O2 and O3. The calculated zero-point energy (ZPE) for the Li_2MSiO_4 polymorphs varies from 0.48 to 0.68 eV/f.u. (see Table S1). Among the studied phases, the *Pbn*2$_1$-Li_2CoSiO_4 and *Pmn*2$_1$-Li_2NiSiO_4 phases have the minimum ZPE value and *I*222-Li_2CoSiO_4 has the maximum value. However, the calculated ZPE for the ambient phases (for example *Pmn*2$_1$, *Pmn*2$_1$-modi, *Pbn*2$_1$ modifications in Li_2MnSiO_4) are very close to each other. This finding suggests that

the exclusion of the temperature effect is not expected to significantly affect our conclusion regarding the transition pressures reported in the present study.

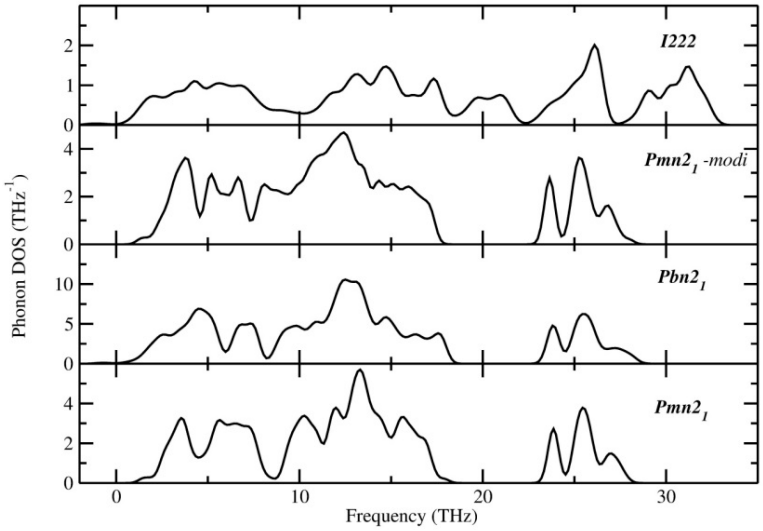

Figure 8. Calculated total phonon density of states for Li_2MnSiO_4 in different modifications. The modifications are noted in the corresponding panel.

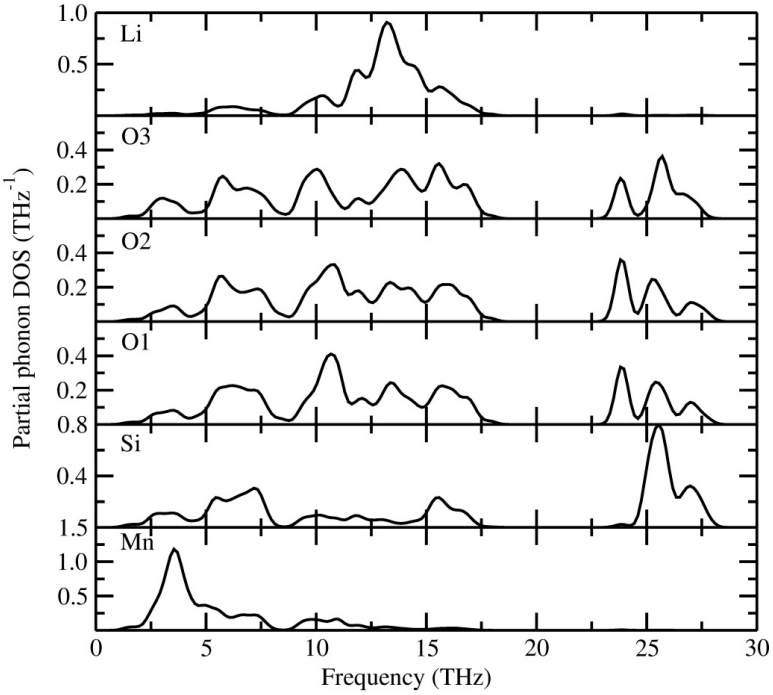

Figure 9. Calculated site projected phonon density of states for Li_2MnSiO_4 in *Pmn*2_1 modification. The corresponding sites are noted in the panel. The oxygen atoms are occupied in three different sites O1(4*a*), O2(2*a*), and O3(2*a*) are marked as O1, O2, and O3 in the figure.

3.4. Single-Crystal Elastic Constants and Mechanical Stability

The absence of imaginary phonon frequencies is not sufficient to validate the overall stability of a certain crystal, as it indicates its stability with respect to positional coordinates, without considering the lattice degrees of freedom. Our study is this completed by evaluating the mechanical stability by computing the single-crystal elastic constants. A set of strains is applied to the crystal cell, and the stress tensor is calculated. The elastic constants are then evaluated by linear fitting of the stress-strain curve.

The elastic constants describe the linear response of a material to an applied deformation, usually described in terms of tensile and shear components. Following the Voigt notation, we write the elastic constants as a 6 × 6 symmetric matrix, having in principle 27 independent components. The stress/strain relation is then written as $S_j = C_{ij}\ \varepsilon_j$ for small stresses, σ, and strains, ε for $i, j = 1, 2, \ldots, 6$ [68].

$$\begin{pmatrix} S_{11} \\ S_{22} \\ S_{33} \\ S_{23} \\ S_{13} \\ S_{12} \end{pmatrix} = \begin{pmatrix} C_{11}C_{12}C_{13}C_{14}C_{15}C_{16} \\ C_{21}C_{22}C_{23}C_{24}C_{25}C_{26} \\ C_{31}C_{32}C_{33}C_{34}C_{35}C_{36} \\ C_{41}C_{42}C_{43}C_{44}C_{45}C_{46} \\ C_{51}C_{52}C_{53}C_{54}C_{55}C_{56} \\ C_{61}C_{62}C_{63}C_{64}C_{65}C_{66} \end{pmatrix} \begin{pmatrix} \varepsilon_{11} \\ \varepsilon_{22} \\ \varepsilon_{33} \\ 2\varepsilon_{23} \\ 2\varepsilon_{13} \\ 2\varepsilon_{12} \end{pmatrix}$$

Structural symmetries simplify the general formula, as the response of the system to different deformation is the same. A cubic crystal, for example, has only three independent elements (C_{11}, C_{12} and C_{44}), each of which represents three equal elastic constants ($C_{11} = C_{22} = C_{33}$; $C_{12} = C_{23} = C_{31}$; $C_{44} = C_{55} = C_{66}$). A single strain with non-vanishing first and fourth components can be used to calculate stresses relating to all three of these coefficients, yielding a very efficient method for obtaining elastic constants. A full account of the symmetry of stress, strain and elastic constants is given by Nye [69].

The elastic constants contain all the information regarding deformation of the crystal, and can be used to evaluate average properties such as the bulk modulus (response to an isotropic compression), the Poisson coefficient, and the Lamé constants, Within the Voigt approximation, the bulk and shear moduli can be written in terms of the elastic constants as:

$$B_{Voigt} = \frac{1}{9}[(C_{11} + C_{22} + C_{33}) + 2(C_{12} + C_{23} + C_{13})] \quad (1)$$

and:

$$G_{Voigt} = \frac{1}{15}\left[(C_{11} + C_{22} + C_{33}) - 2(C_{12} + C_{23} + C_{13}) + \frac{1}{5}(C_{44} + C_{55} + C_{66})\right] \quad (2)$$

alternatively, the Reuss approximation can be used, which relies on the elements of the compliance tensor S_{ij} (the inverse of the stiffness tensor). The bulk modulus is given by:

$$\frac{1}{B_{Reuss}} = [(S_{11} + S_{22} + S_{33}) + 2(S_{12} + S_{23} + C_{13})] \quad (3)$$

and the shear modulus is:

$$\frac{15}{G_{Reuss}} = 4[(S_{11} + S_{22} + S_{33}) - 4(S_{12} + S_{23} + S_{13}) + 3(S_{44} + S_{55} + S_{66})] \quad (4)$$

In general, for polycrystalline materials, the Voigt approximation gives the upper bound on the elastic moduli, while the Reuss approximation gives the lower bound [70]. The two approximations can be averaged in the Voigt-Reuss-Hill (VRH) form for the bulk modulus:

$$B_{VRH} = \frac{B_{Voigt} + B_{Reuss}}{2} \quad (5)$$

the shear modulus:

$$G_{VRH} = \frac{G_{Voigt} + G_{Reuss}}{2} \quad (6)$$

and the Young's modulus (E):

$$E_{VRH} = \frac{9B_{VHR} \times G_{VRH}}{3B_{VHR} + G_{VRH}} \quad (7)$$

The Poisson ratio σ is then obtained by:

$$\sigma = \frac{3B_{VRH} - 2G_{VRH}}{6B_{VRH} + 2G_{VRH}} \tag{8}$$

Using Poisson's ratio, ductility and brittleness of materials may be tested as suggested in reference [71]. For brittle material, σ is below 0.33, while for a ductile material, σ = 0.33.

Lamé constant (λ):

$$\lambda_{VHR} = B_{VHR} - \frac{2G_{VRH}}{3} \tag{9}$$

The quantities can also be used to compute the speed of sound for the transverse and longitudinal waves, using the relations [72] for the speed of sound for the longitudinal waves:

$$v_L = \sqrt{\left(\frac{B + \frac{4}{3}G}{\rho}\right)} \tag{10}$$

and for the transverse waves

$$v_T = \sqrt{\left(\frac{G}{\rho}\right)} \tag{11}$$

where ρ is the mass density of the material. The average speed of sound is then evaluated by

$$\acute{v} = \left[\frac{1}{3}\left(\frac{2}{v_T^3} + \frac{1}{v_L^3}\right)\right]^{\frac{-1}{3}} \tag{12}$$

The Debye temperature of a solid can be written as [53]:

$$\theta_D = \frac{\hbar}{k_B}\left[\frac{6\pi^2 n}{V}\right]^{\frac{1}{3}} \acute{v} \tag{13}$$

where n is the number of atoms in the cell, V is its volume, and $\acute{v}$ is the average speed of sound of Equation (12). In addition to the above mentioned parameters once can also calculate the compressibility of the materials defined as the inverse of the bulk modulus ($1/B_{VHR}$). The ductility i can be estimated by applying Pugh's criteria [73]. According to Pugh, a material is ductile if G_H/B_H is smaller than 0.5, otherwise the material is brittle. The linear fitting of the stress-strain curve has been successfully used to study the elastic response of a range of materials including simple metals (such as Al) [74], super hard nitrides [75], borides [76,77], oxides [78], silicates [79], and semiconductors [80]. The results of these studies show that the accuracy of DFT elastic constants is typically within 10% of the experiment. The calculated values of bulk moduli, shear moduli, Young's moduli and Poisson's ratio are tabulated in Table 3. All these compounds exhibit similar values of the bulk and Young's modulus. The compressibility value of these polymorphs suggested that these compounds are very soft materials. A parameter B/G is also introduced, in which B indicates the bulk modulus and G represent the shear modulus. The bulk and shear moduli are calculated from the Voigt–Reuss–Hill approximations [81–83]. The high (low) G/B value is associated with ductility (brittleness) and the critical value which separates ductile and brittle materials is 0.5 [73]. The calculated G/B values for these compounds are lower than 0.5, implying the ductile characteristics of materials and the stable cycle performance.

In general, the elastic energy of a system subjected to an infinitesimal strain can be written as U = $\varepsilon_i C_{ij} \varepsilon_j$. The system is defined to be stable if U > 0 for every arbitrary strain ε. The elastic constant matrix C_{ij} is therefore required to be positive definite. This proposition is equivalent to any of the following [84]:

1) The eigenvalues of C_{ij} are positive.
2) Every leading principal (or trailing) minor, including determinants of C is positive.

The second condition if also known as Sylvesters critetion. Analytical formula can be readily obtained from these conditions and are reported in literature for simple crystal structures. It is also possible to verify them numerically by means of computational linear algebra routines. This second approach has been followed in this work. The calculated eigenvalues and minors are reported in Table 4 and all are positive for the studied phases. Hence, the studied phases are mechanically stable polymorphs.

Table 4. The calculated eigenvalues and minors of elastic tensor for the studied phases.

Phase	Leading Minors (GPa^n)	Trailing Minors (GPa^n)	Eigenvalues (GPa)
Li_2MnSiO_4-*Pmn*2_1	1.92×10^2 2.02×10^4 2.45×10^6 1.15×10^8 4.29×10^9 2.09×10^{11}	2.09×10^{11} 1.47×10^9 1.28×10^7 8.51×10^4 1.81×10^3 4.86×10^1	2.83×10^2 8.64×10^1 1.00×10^2 4.72×10^1 3.72×10^1 4.86×10^1
Li_2MnSiO_4-*Pmn*2_1-mod	1.19×10^2 1.51×10^4 1.76×10^6 6.53×10^7 2.38×10^9 1.01×10^{11}	1.01×10^{11} 1.06×10^9 7.98×10^6 5.76×10^4 1.55×10^3 4.26×10^1	2.34×10^2 7.92×10^1 9.54×10^1 4.24×10^1 3.53×10^1 3.83×10^1
Li_2MnSiO_4-*Pbn*2_1	1.24×10^2 1.52×10^4 1.88×10^6 6.85×10^7 2.56×10^9 1.09×10^{11}	1.09×10^{11} 1.20×10^9 9.05×10^6 5.81×10^4 1.59×10^3 4.25×10^1	2.67×10^2 7.24×10^1 9.70×10^1 3.65×10^1 3.74×10^1 4.25×10^1
Li_2MnSiO_4-*I*222	3.12×10^2 7.24×10^4 1.13×10^7 1.09×10^8 6.12×10^9 1.39×10^{10}	1.39×10^{10} 2.09×10^8 2.42×10^6 2.93×10^4 8.74×10^2 3.31×10^1	6.37×102 1.64×102 1.35×102 8.07×10^1 1.24 9.87
Li_2CoSiO_4-*Pmn*2_1	1.83×10^2 1.94×10^4 2.20×10^6 1.04×10^8 4.30×10^9 1.85×10^{11}	1.85×10^{11} 1.23×10^9 1.10×10^7 8.39×10^4 1.77×10^3 4.29×10^1	2.46×10^2 1.02×10^2 8.73×10^1 4.75×10^1 4.12×10^1 4.29×10^1
Li_2CoSiO_4-*Pmn*2_1-modi	9.64×101 1.05×10^4 1.07×10^6 4.45×10^7 1.51×10^9 6.57×10^{10}	6.57×10^{10} 8.20×10^8 7.11×10^6 6.19×10^4 1.48×10^3 4.37×10^1	1.78×10^2 4.33×10^1 6.74×10^1 8.94×10^1 3.38×10^1 4.19×10^1
Li_2CoSiO_4-*Pbn*2_1	1.19×10^2 1.44×10^4 1.64×10^6 7.66×10^7 2.84×10^9 1.24×10^{11}	1.24×10^{11} 1.29×10^9 9.90×10^6 7.53×10^4 1.62×10^3 4.36×10^1	2.16×10^2 7.74×10^1 9.81×10^1 4.66×10^1 3.71×10^1 4.36×10^1
Li_2CoSiO_4-*I*222	2.02×10^2 3.72×10^4 7.88×10^5 4.72×10^7 3.55×10^9 2.66×10^{11}	2.66×10^{11} 2.49×10^9 2.19×10^7 3.38×10^5 5.64×10^3 7.51×10^1	3.09×10^2 1.42×10^2 1.80×10^1 6.00×10^1 7.51×10^1 7.51×10^1
Li_2NiSiO_4-*P*2_1	1.35×10^2 1.37×10^4 1.66×10^6 7.54×10^7 3.15×10^9 1.59×10^{11}	1.59×10^{11} 1.56×10^9 1.55×10^7 1.03×10^5 2.28×10^3 5.43×10^1	2.41×10^2 4.87×10^1 8.11×10^1 8.79×10^1 4.75×10^1 4.01×10^1
Li_2NiSiO_4-*P*$2_1/n$	1.37×10^2 1.34×10^4 1.53×10^6 6.69×10^7 2.97×10^9 1.48×10^{11}	1.48×10^{11} 1.39×10^9 1.43×10^7 1.05×10^5 2.41×10^3 5.40×10^1	2.29×10^2 4.77×10^1 8.13×10^1 8.57×10^1 4.74×10^1 4.11×10^1
Li_2NiSiO_4-*Pmn*2_1	2.03×10^2 2.20×10^4 2.53×10^6 1.19×10^8 4.67×10^9 2.12×10^{11}	2.12×10^{11} 1.21×10^9 1.11×10^7 8.39×10^4 1.78×10^3 4.54×10^1	2.54×10^2 1.12×10^2 8.91×101 4.72×10^1 3.92×10^1 4.54×10^1
Li_2NiSiO_4-*I*222	2.01×10^2 2.66×10^4 2.43×10^5 1.80×10^7 1.17×10^9 7.86×10^{10}	7.86×10^{10} 1.36×10^9 1.58×10^7 3.24×10^5 4.38×10^3 6.74×10^1	2.89×10^2 1.07×10^2 7.83 7.40×10^1 6.49×10^1 6.74×10^1

3.5. Diffusion Coefficient and Ionic Conductivity

We describe here the diffusion pathways for the transport of Li^+ ions and the associated activation energies. The latter quantities are evaluated using the NEB method, and the diffusion coefficients D are then obtained using the equation:

$$D = d^2 \vartheta_0 exp\left(\frac{-E_a}{k_B T}\right) \quad (14)$$

where d is the hopping distance, E_a the activation energy, k_B the Boltzmann constant, T the temperature and the attempt frequency (assumed to be 10^{13} Hz). In our extensive work on the diffusion of Li/Na within electrolyte or electrode materials, we have always found that converged results are obtained with 5 intermediate images for the neb calculations, for a total of 7 images considering the starting and the final configurations. According to our experience, calculations using an odd number of images converge more rapidly to the correct activation energy. This is due to the fact that, if the initial and final minima are equivalent, the saddle point if often located in the middle position, corresponding to the $(n + 1)/2$ position where n is the total number of images. With this in mind, we have reproduced one of our calculations (the first hop within the Li_2MnSiO_4 structure) using seven intermediate images. The comparison between these simulations is reported in Figure S6. The cubic splines, computed using the forces resulting from the NEB calculations, are indicated with solid lines, while the energy of the minima and of intermediate configurations are indicated with dots. As can be noted, the two splines are nearly overlapping, and the position of the saddle point and the associated energy (i.e., the activation barrier) are in perfect agreement. Hence, in the rest of the configurations we have used only five intermediate images.

The structures of Li_2MSiO_4 materials obtained from different synthesis methods further affect the lithium intercalation behavior [85], The calculated diffusion barriers for the low energy structures of the studied phases are listed in Table 5. In this section, we present only the low energy configurations of the Li_2MSiO_4 materials with more details. In the case of Li_2MnSiO_4, all the lithium ions are located at 4*b* Wyckoff sites. Two hops are found to regulate the diffusion along this network. These are labelled as (i) and (ii) and are indicated in Figure 10a using ball and stick models. These hops have length 3.12 and 3.18 Å respectively, and associated activation energies of 0.78 and 0.86 eV respectively (see Figure 11a). The associated energy curves along the MEP are displayed in Figure 11a, with yellow and green lines respectively. As clear from Figure 10a, the diffusion along the ***c*** direction is regulated only by type (i) hops, whereas diffusion along *a* by type (ii) segments. Diffusion along *b* is not considered within our model, as the hop required to form a percolating path along this direction would have a length larger than 4 Å, and it is therefore unlikely to occur. These calculation reveal Li_2MnSiO_4 as a mediocre 2D conductor of Li ions.

In the case Li_2CoSiO_4, two inequivalent Li atoms are found, both located at 4*a* Wyckoff positions, indicated in Figure 10b using yellow and green spheres. Sticks connecting spheres indicate the possible hops for a Li vacancy within a 4 Å cutoff. Only hops connecting inequivalent Li atoms are available. Three inequivalent hops are found, labelled (i), (ii), and (iii) in Figure 10b with respective lengths of 2.99, 3.08, and 3.26 Å. The activation barriers for vacancy hopping along these distances are calculated to be 0.42, 0.71, and 0.85 eV. The energy curve along the MEP is reported in Figure 10b for these hops in green, blue, and yellow, respectively. Note that the extrema of these curves are shifted with respect to each other, indicating that the formation of a vacancy at site 1 (green sphere) is more favourable by 0.17 eV. These segments are used to construct percolating paths, considered to model the diffusion of Li atoms along independent directions. Indeed, the activation energies are to be anisotropic. Diffusion along the *a* direction is described defining two distinct percolating paths, as clear from Figure 10b. The first path is comprised by hops (i) and (iii), and the second one by (ii) and (iii). Due to the fact that hop (iii) is included in both both and it is the one with largest associated diffusion barrier, we can conclude that the activation energy for diffusion along *a* is 0.85 eV. While diffusion along *b* is

regulated by the same processes, a third percolating path, comprised by (ii) hops only, best describes diffusion along the ***c*** direction. The associated activation energy in this case is found to be 0.71 eV (see Figure 11b). Taking all together, Li_2CoSiO_4 is found to be a mediocre conductor of Li ions.

Table 5. Calculated barrier height (in eV), Li-Li migration distance (in Å), and diffusion coefficient (D; $cm^2\ s^{-1}$) for Li_2MSiO_4 phases.

Phase	Barrier Height	Li-Li Distance	Diffusion Coefficient at 300 K
Li_2MnSiO_4-*Pmn*2_1	0.78 0.86	3.12 3.18	7.6×10^{-16} 3.6×10^{-18}
Li_2MnSiO_4-*Pbn*2_1	0.68 0.70 0.73	3.03 3.09 3.12	3.4×10^{-15} 1.6×10^{-15} 5.3×10^{-16}
Li_2MnSiO_4-*I*222	1.2 1.23	3.12 3.20	6.7×10^{-24} 2.2×10^{-24}
Li_2CoSiO_4-*Pbn*2_1	0.43 0.75 0.86	2.99 3.08 3.26	5.3×10^{-10} 2.4×10^{-15} 3.8×10^{-17}
Li_2CoSiO_4-*Pmn*2_1-mod	0.74 0.79	3.24 3.33	3.9×10^{-16} 5.9×10^{-17}
Li_2CoSiO_4-*I*222	1.1 1.31	3.03 3.31	3.0×10^{-22} 1.08×10^{-25}
Li_2NiSiO_4-*P*2_1	0.67 0.74 0.74 0.77	2.72 3.09 3.10 3.24	4.1×10^{-15} 3.5×10^{-16} 3.5×10^{-16} 1.2×10^{-16}
Li_2NiSiO_4-*Pmn*2_1	0.85 0.89	3.12 3.27	5.1×10^{-18} 1.2×10^{-18}
Li_2NiSiO_4-*I*222	1.07 1.12	3.12 3.27	1.0×10^{-21} $1.6 \times a10^{-22}$

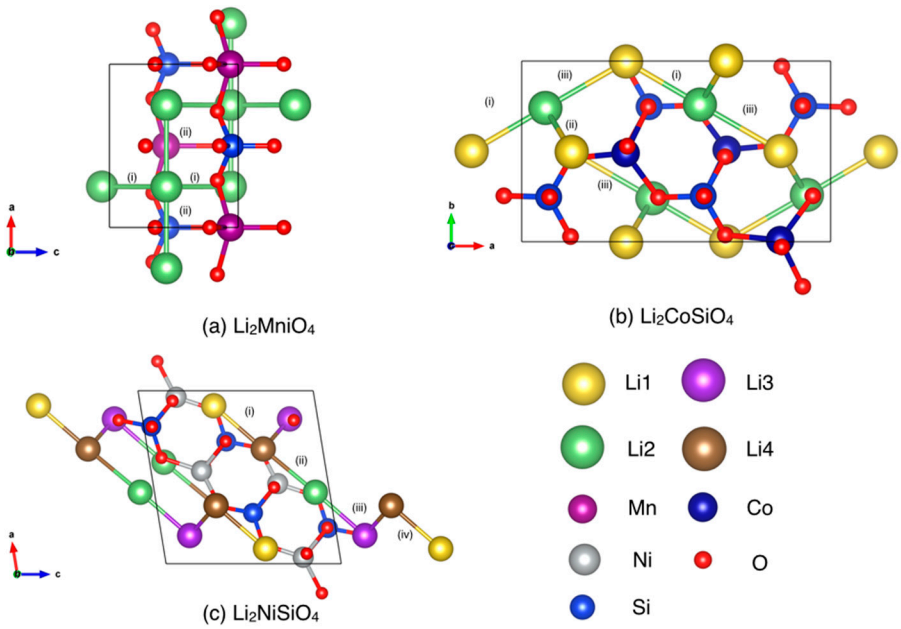

Figure 10. Li ion migration in different possible pathways (represented as i, ii, etc.) in (**a**) Li_2MnSiO_4 (*Pmn*2_1), (**b**) Li_2CoSiO_4 (*Pbn*2_1), and (**c**) Li_2NiSiO_4 (*P*2_1) used for NEB simulation.

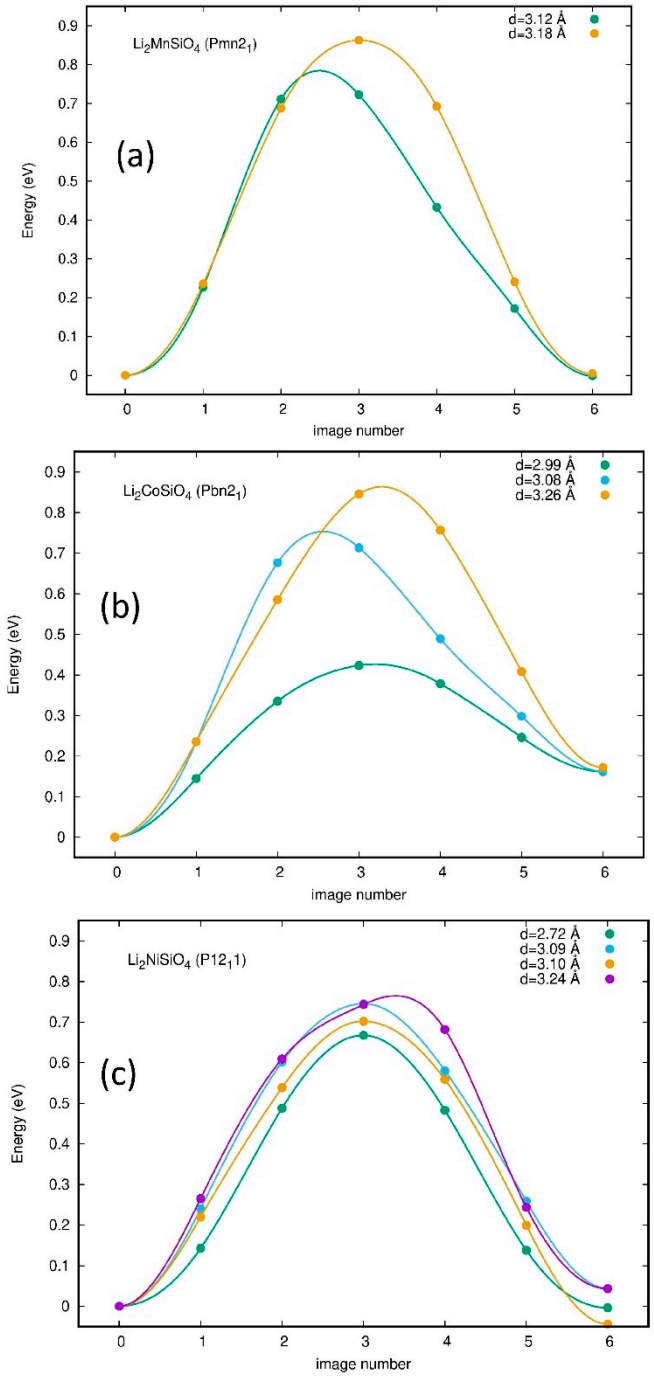

Figure 11. Li ion migration in different possible path ways in (**a**) Li_2MnSiO_4 ($Pmn2_1$), (**b**) Li_2CoSiO_4 ($Pbn2_1$), and (**c**) Li_2NiSiO_4 ($P2_1$) obtained from NEB method. The connected lines are just to give a visual help of the sequence of images. The symbols represent calculated data points.

In the case of Li_2NiSiO_4, the Li atoms are located at four inequivalent 2*a* Wyckoff sites, indicated in Figure 10c with green, yellow, purple and brown spheres. The vacancy formation energies for these atoms are comparable, being within a 50 meV energy window, and diffusion along the while network is possible. We have considered four hops within this Li frame connecting frame, with length smaller than 4 Å. The first one, labelled as (i) and indicated in Figure 10c using a stick connecting spheres, connects Li1 and Li3, indicated with green and purple spheres respectively. The hop length is 3.11 Å, and the associated activation energy 0.74 eV. The second hop, connects Li1 and Li4, the latter indicated with a brown sphere, and has an activation energy of 0.74 eV.

We then considered hop three, between Li3 and Li4, with a length of 2.72 Å and an activation energy of 0.67 eV and hop four, between Li4 and Li2, with a length of 3.10 Å an activation energy of 0.74 eV (see Figure 11c). The ensemble of these hops form a percolating path within this layered structure, as clear from Figure 10c. The activation energy for Li-ion diffusion is therefore calculated to be 0.74 eV. In Figure 12 the results obtained for the natural logarithm of the diffusion coefficient in the low energy structures of Li_2MSiO_4 phases are displayed as a function of 1/T. The activation barrier is proportional to the slope of each straight line. The diffusion coefficient calculated in Li_2MSiO_4 polymorphs at room temperature, ranges from 10^{-25} cm^2/s up to 10^{-16} cm^2/s. On the other hand, the diffusion coefficient in commercial materials (e.g., Li_xCoO_2) is typically ranging from 10^{-13} cm^2/s to 10^{-7} cm^2/s. It is then clear that Li_2MSiO_4 phases cannot provide at the moment better kinetics than the state-of-the-art materials. However, by tailoring the particle size of the Li_2FeSiO_4 one can reduce the diffusion coefficient below 10^{-7} cm^2/s [86]. A similar effect can be expected on these studied phases and the investigation is under progress.

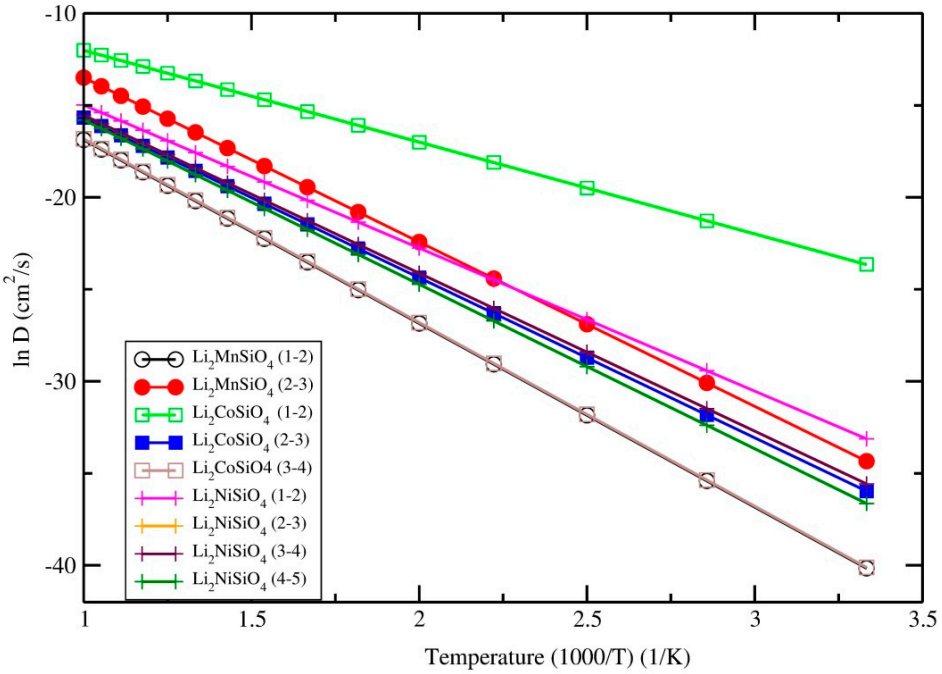

Figure 12. Natural logarithm of the diffusion coefficient against 1/T for different possible path ways in Li_2MnSiO_4 ($Pmn2_1$), Li_2CoSiO_4 ($Pbn2_1$), and Li_2NiSiO_4 ($P2_1$) obtained from NEB method. For the clarity of the figure only equilibrium structures natural logarithm of the diffusion coefficient against 1/T are shown in the figure.

4. Conclusions

In summary, the relative stability of Li_2MSiO_4 (M = Mn, Co, and Ni), electronic, lattice dynamics, mechanical, and electrochemical properties have been investigated, using density functional theory within the GGA approximation plus on-site Coulomb energy correction (U). According to our theoretical simulation, at ambient condition, Li_2MSiO_4, Li_2CoSiO_4, and Li_2NiSiO_4 are stabilized in the $Pmn2_1$, $Pbn2_1$, and $P2_1$ structures, respectively. When an external pressure is applied, the ground state structure of Li_2MnSiO_4 in $Pmn2_1$ transforms into the $I222$ modification at 8.2 GPa. For Li_2CoSiO_4, the following phase transition sequence was identified; $Pbn2_1 \rightarrow Pmn2_1$-mod $\rightarrow Pmn2_1 \rightarrow I222$ at 1.4, 5.4 and 20.5 GPa respectively. Similarly, for Li_2NiSiO_4 phase the following path was identified $P2_1 \rightarrow Pmn2_1 \rightarrow I222$ and the involved pressures are 0.7, and 15.9 GPa, respectively. The calculated structural data for these known phases are fitted very well with the experimental as well as other theoretical reports available in the literature. For all these compounds, several structures coexist within a very small energy window.

This proximity in energy clearly indicates that, depending upon the method of synthesis, one can stabilise either of these phases at ambient conditions and it might be a very challenging task for the experimentalist to get a phase pure sample. Furthermore, our vibrational analysis and single crystal elastic constant study clearly indicates that all these phases are dynamically as well as mechanically stable phases. Hence, one is more likely to obtain -multiphase materials. This might be solvable by a proper annealing procedure. However, during the battery cycling process these multiphases may form and the quantities of the phases may vary by the internal potential as well as chemical environment. The electronic structure of these phases revealed that all these compounds exhibit a finite energy gap between the valance and the conduction band. Hence, these compounds exhibit a poor electronic conductivity. Once the materials' get amorphization or structural collapse were inhibited during lithium ion insertion/extraction from the host lattice, reversible structural changes and good cycling performances could be attained. Hence, it is important to understand the role of ion-substitution (either by one of the *M* atom or partial substitution of other transition metal), for stabilizing the structures, is an effective way to achieve high-capacity Li_2MSiO_4 materials. The work is under progress and the result will be publish in the forth coming article. Material-coating and optimization of the particle size/morphology are also applied as exterior modifying methods to enhance the electrochemical performance. From NEB calculation we found that the diffusion coefficients in Li_2MSiO_4 at room temperature are ranging from 10^{-25} cm^2/s up to 10^{-10} cm^2/s. The ionics is therefore suboptimal with respect to the current generation of state-of-the-art materials. More work is therefore required in order to improve the Li-ion diffusion in this class of materials.

Supplementary Materials: The following are available online at http://www.mdpi.com/1996-1073/12/2/224/s1, Figure S1: Calculated electronic up-spin [(**a**) and (**c**)] and down-spin [(**b**) and (**d**)] band structure of Li_2MnSiO_4 in $Pmn2_1$ phase with [(**a**) and (**b**)] and without GGA+*U* correction [(**c**) and (**d**)]. The Fermi level is set to zero and marked by dotted line. The band gap value is changed from 2.1 eV to 2.9 eV when we include the GGA+*U* correction, Figure S2: Calculated electronic up-spin and down-spin band structure of Li_2MnSiO_4 in $P2/n$, $P2_1$, and $I\text{-}42m$ phases. The Fermi level is set to zero and marked by dotted line, Figure S3: Calculated electronic up-spin and down-spin band structure of Li_2CoSiO_4 in Pn, $Pbn2_1$, and $I\text{-}42m$ phases. The Fermi level is set to zero and marked by dotted line, Figure S4: Calculated electronic up-spin and down-spin band structure of Li_2NiSiO_4 in $P2/n$, $Pmn2_1$, $P2_1$, and $I\text{-}42m$ phases. The Fermi level is set to zero and marked by dotted line, Figure S5: Calculated total phonon density of states for Li_2CoSiO_4 and Li_2NiSiO_4 in different modifications. The modifications are noted in the corresponding panel, Figure S6: Comparison between the energetics along the minimum energy path calculated using 5 and 7 intermediate images, Table S1: Computational details for the phonon calculation, calculated zero-point energy (ZPE) from the phonon density of states for different Li_2MSiO_4 polymorphs.

Author Contributions: Conceptualization, P.V.; methodology, P.V.; formal analysis, P.V and F.B.; investigation, P.V.; writing—original draft preparation, P.V.; writing—review and editing, P.V and F.B.; project administration, H.F.; funding acquisition, H.F.

Funding: This research was funded by Research Council of Norway, Grant agreement no.: Nano-MILIB-143732 and SELiNaB-255441.

Acknowledgments: P.V. acknowledges the Research Council of Norway for providing the computer time (under the project number NN2875k and NS2875k) at the Norwegian supercomputer (UNINETT Sigma2 AS).

Conflicts of Interest: The authors declare no conflict of interest.

References

1. Winter, M.; Brodd, R.J. What Are Batteries, Fuel Cells, and Supercapacitors? *Chemical Rev.* **2004**, *104*, 4245–4270. [CrossRef]
2. Dippel, C.; Krueger, S.; Kloepsch, R.; Niehoff, P.; Hoffmann, B.; Nowak, S.; Passerini, S.; Winter, M.; Li, J. Aging of Li_2FeSiO_4 cathode material in fluorine containing organic electrolytes for lithium-ion batteries. *Electrochim. Acta* **2012**, *85*, 66–71. [CrossRef]
3. Whittingham, M.S. Lithium batteries and cathode materials. *Chem. Rev.* **2004**, *104*, 4271–4301. [CrossRef] [PubMed]
4. Nytén, A.; Abouimrane, A.; Armand, M.; Gustafsson, T.; Thomas, J.O. Electrochemical performance of Li2FeSiO4 as a new Li-battery cathode material. *Electrochem. Commun.* **2005**, *7*, 156–160. [CrossRef]

5. Dominko, R.; Bele, M.; Gaberšček, M.; Meden, A.; Remškar, M.; Jamnik, J. Structure and electrochemical performance of Li_2MnSiO_4 and Li_2FeSiO_4 as potential Li-battery cathode materials. *Electrochem. Commun.* **2006**, *8*, 217–222. [CrossRef]
6. Zaghib, K.; Salah, A.; Ravet, N.; Mauger, A.; Gendron, F.; Julien, C. Structural, magnetic and electrochemical properties of lithium iron orthosilicate. *J. Power Sources* **2006**, *160*, 1381–1386. [CrossRef]
7. Quoirin, G.; Taulelle, F.; Dupont, L.; Masquelier, C. Crystal Chemistry and Electrochemical Delithiation of Li_2FeSiO_4. In Proceedings of the 211th ECS Meeting, Chicago, IL, USA, 6–10 May 2007.
8. Sirisopanaporn, C.; Boulineau, A.; Hanzel, D.; Dominko, R.; Budic, B.; Armstrong, A.R.; Bruce, P.G.; Masquelier, C. Crystal structure of a new polymorph of Li_2FeSiO_4. *Inorg. Chem.* **2010**, *49*, 7446–7451. [CrossRef]
9. Arroyo-de Dompablo, M.E.; Armand, M.; Tarascon, J.M.; Amador, U. On-demand design of polyoxianionic cathode materials based on electronegativity correlations: An exploration of the Li_2MSiO_4 system (M = Fe, Mn, Co, Ni). *Electrochem. Commun.* **2006**, *8*, 1292–1298. [CrossRef]
10. Islam, M.S.; Dominko, R.; Masquelier, C.; Sirisopanaporn, C.; Armstrong, A.R.; Bruce, P.G. Silicate cathodes for lithium batteries: Alternatives to phosphates? *J. Mater. Chem.* **2011**, *21*, 9811–9818. [CrossRef]
11. Longo, R.C.; Xiong, K.; Cho, K. First Principles Study of Multicomponent Silicate Materials for Rechargeable Li-Ion Batteries. *ECS Trans.* **2012**, *41*, 75–85. [CrossRef]
12. Deng, C.; Zhang, S.; Fu, B.L.; Yang, S.Y.; Ma, L. Characterization of Li_2MnSiO_4 and Li_2FeSiO_4 cathode materials synthesized via a citric acid assisted sol–gel method. *Mater. Chem. Phys.* **2010**, *120*, 14–17. [CrossRef]
13. Zhu, X.; Chen, N.; Lian, F.; Song, Y.; Li, Y. First principle calculation of lithiation/delithiation voltage in Li-ion battery materials. *Chin. Sci. Bull.* **2011**, *56*, 3229. [CrossRef]
14. Tsubakiyama, K.; Kudo, Y.; Yamashita, K. First-Principles Study on Li2MSiO4 (M = Mn, Fe, Co, Ni) as Cathode Materials of Lithium Ion Battery. *ECS Trans.* **2013**, *53*, 25–34. [CrossRef]
15. Larsson, P.; Ahuja, R.; Nytén, A.; Thomas, J.O. An ab initio study of the Li-ion battery cathode material Li_2FeSiO_4. *Electrochem. Commun.* **2006**, *8*, 797–800. [CrossRef]
16. Nyten, A.; Kamali, S.; Haggstrom, L.; Gustafsson, T.; Thomas, J.O. The lithium extraction/insertion mechanism in Li_2FeSiO_4. *J. Mater. Chem.* **2006**, *16*, 2266–2272. [CrossRef]
17. Romain, G.; Pluton, P.; François-Xavier, C. ELATE: An open-source online application for analysis and visualization of elastic tensors. *J. Phys. Condens. Matter* **2016**, *28*, 275201.
18. Vajeeston, P.; Fjellvag, H. First-principles study of structural stability, dynamical and mechanical properties of Li_2FeSiO_4 polymorphs. *RSC Adv.* **2017**, *7*, 16843–16853. [CrossRef]
19. Longo, R.C.; Xiong, K.; Wang, W.; Cho, K. Influence of the exchange-correlation potential on the electrochemical properties of multicomponent silicate cathode materials. *Electrochim. Acta* **2012**, *80*, 84–89. [CrossRef]
20. Wu, S.Q.; Zhu, Z.Z.; Yang, Y.; Hou, Z.F. Structural stabilities, electronic structures and lithium deintercalation in LixMSiO4 (M = Mn, Fe, Co, Ni): A GGA and GGA + U study. *Comput. Mater. Sci.* **2009**, *44*, 1243–1251. [CrossRef]
21. Liivat, A.; Thomas, J.O. Li-ion migration in Li_2FeSiO_4-related cathode materials: A DFT study. *Solid State Ion.* **2011**, *192*, 58–64. [CrossRef]
22. Zhong, G.; Li, Y.; Yan, P.; Liu, Z.; Xie, M.; Lin, H. Structural, Electronic, and Electrochemical Properties of Cathode Materials Li_2MSiO_4 (*M* = Mn, Fe, and Co): Density Functional Calculations. *J. Phys. Chem. C* **2010**, *114*, 3693–3700. [CrossRef]
23. Li, L.; Zhu, L.; Xu, L.-H.; Cheng, T.-M.; Wang, W.; Li, X.; Sui, Q.-T. Site-exchange of Li and M ions in silicate cathode materials Li_2MSiO_4 (M = Mn, Fe, Co and Ni): DFT calculations. *J. Mater. Chem. A* **2014**, *2*, 4251–4255. [CrossRef]
24. Kalantarian, M.M.; Asgari, S.; Capsoni, D.; Mustarelli, P. An ab initio investigation of $Li_2M_{0.5}N_{0.5}SiO_4$ (M, N = Mn, Fe, Co Ni) as Li-ion battery cathode materials. *Phys. Chem. Chem. Phys.* **2013**, *15*, 8035–8041. [CrossRef] [PubMed]
25. Zhang, P.; Li, X.D.; Yu, S.; Wu, S.Q.; Zhu, Z.Z.; Yang, Y. Effects of Na Substitution on Li Ion Migration in Li2CoSiO4 Cathode Material. *J. Electrochem. Soc.* **2013**, *160*, A658–A661. [CrossRef]
26. Bianchini, F.; Fjellvåg, H.; Vajeeston, P. First-principles study of the structural stability and electrochemical properties of Na_2MSiO_4 (M = Mn, Fe, Co and Ni) polymorphs. *Phys. Chem. Chem. Phys.* **2017**, *19*, 14462–14470. [CrossRef]

27. Santamaría-Pérez, D.; Amador, U.; Tortajada, J.; Dominko, R.; Arroyo-de Dompablo, M.E. High-Pressure Investigation of Li_2MnSiO_4 and Li_2CoSiO_4 Electrode Materials for Lithium-Ion Batteries. *Inorg. Chem.* **2012**, *51*, 5779–5786. [CrossRef]
28. Armand, M. Method for Synthesis of Carbon-Coated Redox Materials with Controlled Size. World Patent WO02/27823, 4 April 2002.
29. Feng, Y.; Ji, R.; Ding, Z.; Zhang, D.; Liang, C.; Chen, L.; Ivey, D.G.; Wei, W. Understanding the Improved Kinetics and Cyclability of a Li_2MnSiO_4 Cathode with Calcium Substitution. *Inorg. Chem.* **2018**, *57*, 3223–3231. [CrossRef]
30. Wang, C.; Xu, Y.; Sun, X.; Zhang, B.; Chen, Y.; He, S. Enhanced electrochemical properties of F-doped Li_2MnSiO_4/C for lithium ion batteries. *J. Power Sources* **2018**, *378*, 345–352. [CrossRef]
31. Zhang, Z.; Chen, Z.; Zhang, X.; Wu, D.; Li, J. P-doping Li_2CoSiO_4/C cathode material: A joint experimental and theoretical study. *Electrochim. Acta* **2018**, *264*, 166–172. [CrossRef]
32. Du, H.; Zhang, X.; Chen, Z.; Wu, D.; Zhang, Z.; Li, J. Carbon coating and Al-doping to improve the electrochemistry of Li_2CoSiO_4 polymorphs as cathode materials for lithium-ion batteries. *RSC Adv.* **2018**, *8*, 22813–22822. [CrossRef]
33. Kresse, G.; Furthmüller, J. Efficient iterative schemes for ab initio total-energy calculations using a plane-wave basis set. *Phys. Rev. B* **1996**, *54*, 11169–11186. [CrossRef]
34. Kresse, G.; Furthmuller, J. Efficiency of ab-initio total energy calculations for metals and semiconductors using a plane-wave basis set. *Comput. Mater. Sci.* **1996**, *6*, 15–50. [CrossRef]
35. Perdew, J.P.; Burke, K.; Ernzerhof, M. Generalized Gradient Approximation Made Simple. *Phys. Rev. Lett.* **1996**, *77*, 3865–3868. [CrossRef] [PubMed]
36. Liechtenstein, A.I.; Anisimov, V.I.; Zaanen, J. Density-functional theory and strong interactions: Orbital ordering in Mott-Hubbard insulators. *Phys. Rev. B* **1995**, *52*, R5467–R5470. [CrossRef]
37. Dudarev, S.L.; Botton, G.A.; Savrasov, S.Y.; Szotek, Z.; Temmerman, W.M.; Sutton, A.P. Electronic Structure and Elastic Properties of Strongly Correlated Metal Oxides from First Principles: LSDA + U, SIC-LSDA and EELS Study of UO_2 and NiO. *Phys. Status Solidi A* **1998**, *166*, 429–443. [CrossRef]
38. Vinet, P.; Rose, J.H.; Ferrante, J.; Smith, J.R. Temperature effects on the universal equation of state of solids. *J. Phys. Condens. Matter* **1989**, *1*, 1941–1963. [CrossRef]
39. Vajeeston, P.; Ravindran, P.; Fjellvåg, H. Novel High Pressure Phases of β-AlH3: A Density-Functional Study. *Chem. Mater.* **2008**, *20*, 5997–6002. [CrossRef]
40. Togo, A.; Oba, F.; Tanaka, I. First-principles calculations of the ferroelastic transition between rutile-type and SiO_2 at high pressures. *Phys. Rev. B* **2008**, *78*, 134106. [CrossRef]
41. Monkhorst, H.J.; Pack, J.D. Special points for Brillouin-zone integrations. *Phys. Rev. B* **1976**, *13*, 5188–5192. [CrossRef]
42. Jonsson, H.; Mills, G.; Jacobsen, K.W. Nudged elastic band method for finding minimum energy paths of transitions. In *Classical and Quantum Dynamics in Condensed Phase Simulations*; World Scientific: Singapore, 2011; pp. 385–404. [CrossRef]
43. Henkelman, G.; Jónsson, H. Improved tangent estimate in the nudged elastic band method for finding minimum energy paths and saddle points. *J. Chem. Phys.* **2000**, *113*, 9978–9985. [CrossRef]
44. *Inorganic Crystal Structure Database (ICSD)*; Version 2011/2; Fachinformationszentrum Karlsruhe: Karlsruhe, Germany, 2011.
45. Vajeeston, P.; Ravindran, P.; Kjekshus, A.; Fjellvåg, H. Crystal structure of $KAlH_4$ from first principle calculations. *J. Alloy. Compd.* **2004**, *363*, L8–L12. [CrossRef]
46. Vajeeston, P.; Ravindran, P.; Hauback, B.C.; Fjellvag, H. Prediction of crystal structure, lattice dynamical, and mechanical properties of CaB_2H_2. *Int. J. Hydrogen Energy* **2011**, *36*, 10149–10158. [CrossRef]
47. Vajeeston, P.; Ravindran, P.; Kjekshus, A.; Fjellvåg, H. First-principles investigations of the $MMgH_3$ (M = Li, Na, K, Rb, Cs) series. *J. Alloy. Compd.* **2008**, *450*, 327–337. [CrossRef]
48. Sirisopanaporn, C.; Masquelier, C.; Bruce, P.G.; Armstrong, A.R.; Dominko, R. Dependence of Li_2FeSiO_4 electrochemistry on structure. *J. Am. Chem. Soc.* **2011**, *133*, 1263–1265. [CrossRef]
49. Yabuuchi, N.; Yamakawa, Y.; Yoshii, K.; Komaba, S. Hydrothermal Synthesis and Characterization of Li_2FeSiO_4 as Positive Electrode Materials for Li-Ion Batteries. *Electrochemistry* **2010**, *78*, 363–366. [CrossRef]
50. Huang, X.; Li, X.; Wang, H.; Pan, Z.; Qu, M.; Yu, Z. Synthesis and electrochemical performance of Li_2FeSiO_4/carbon/carbon nano-tubes for lithium ion battery. *Electrochim. Acta* **2010**, *55*, 7362–7366. [CrossRef]

51. Qu, L.; Fang, S.H.; Yang, L.; Hirano, S. Synthesis and characterization of high capacity Li_2MnSiO_4/C cathode material for lithium-ion battery. *J. Power Sources* **2014**, *252*, 169–175. [CrossRef]
52. Shao, B.; Taniguchi, I. Synthesis of Li_2MnSiO_4/C nanocomposites for lithium battery cathode employing sucrose as carbon source. *Electrochim. Acta* **2014**, *128*, 156–162. [CrossRef]
53. Choi, J.-J.; Kim, S.; Im, W.-B.; Chang, W.; Cho, B.-W.; Kim, J.H.; Choi, H.-L.; Chung, K.Y. Synthesis of nanostructured Li_2MnSiO_4/C using a microwave assisted sol–gel process with water as a base solvent. *J. Electroceramics* **2013**, *31*, 176–180. [CrossRef]
54. Ghosh, P.; Mahanty, S.; Basu, R.N. Improved Electrochemical Performance of Li_2MnSiO_4/C Composite Synthesized by Combustion Technique. *J. Electrochem. Soc.* **2009**, *156*, A677–A681. [CrossRef]
55. Politaev, V.V.; Petrenko, A.A.; Nalbandyan, V.B.; Medvedev, B.S.; Shvetsova, E.S. Crystal structure, phase relations and electrochemical properties of monoclinic Li_2MnSiO_4. *J. Solid State Chem.* **2007**, *180*, 1045–1050. [CrossRef]
56. Duncan, H.; Kondamreddy, A.; Mercier, P.H.J.; Le Page, Y.; Abu-Lebdeh, Y.; Couillard, M.; Whitfield, P.S.; Davidson, I.J. Novel Pn Polymorph for Li_2MnSiO_4 and Its Electrochemical Activity As a Cathode Material in Li-Ion Batteries. *Chem. Mater.* **2011**, *23*, 5446–5456. [CrossRef]
57. Zhang, S.; Deng, C.; Fu, B.L.; Yang, S.Y.; Ma, L. Doping effects of magnesium on the electrochemical performance of Li_2FeSiO_4 for lithium ion batteries. *J. Electroanal. Chem.* **2010**, *644*, 150–154. [CrossRef]
58. Arroyo-de Dompablo, M.; Dominko, R.; Gallardo-Amores, J.; Dupont, L.; Mali, G.; Ehrenberg, H.; Jamnik, J.; Moran, E. On the Energetic Stability and Electrochemistry of Li_2MnSiO_4 Polymorphs. *Chem. Mater.* **2008**, *20*, 5574–5584. [CrossRef]
59. Eames, C.; Armstrong, A.R.; Bruce, P.G.; Islam, M.S. Insights into Changes in Voltage and Structure of Li_2FeSiO_4 Polymorphs for Lithium-Ion Batteries. *Chem. Mater.* **2012**, *24*, 2155–2161. [CrossRef]
60. Saracibar, A.; Van der Ven, A.; Arroyo-de Dompablo, M.E. Crystal Structure, Energetics, And Electrochemistry of Li_2FeSiO_4 Polymorphs from First Principles Calculations. *Chem. Mater.* **2012**, *24*, 495–503. [CrossRef]
61. Yamaguchi, H.; Akatsuka, K.; Setoguchi, M.; Takaki, Y. Structure of cobalt dilithium silicate β_{II}-Li_2CoSiO_4. *Acta Crystallogr. Sect. B* **1979**, *35*, 2680–2682. [CrossRef]
62. Arroyo y de Dompablo, M.E.; Amador, U.; Gallardo-Amores, J.M.; Morán, E.; Ehrenberg, H.; Dupont, L.; Dominko, R. Polymorphs of Li_3PO_4 and Li_2MSiO_4 (M = Mn, Co): The role of pressure. *J. Power Sources* **2009**, *189*, 638–642. [CrossRef]
63. West, A.R.; Glasser, F.P. Preparation and crystal chemistry of some tetrahedral Li_3PO_4-type compounds. *J. Solid State Chem.* **1972**, *4*, 20–28. [CrossRef]
64. Yamaguchi, H.; Akatsuka, K.; Setoguchi, M. Structure of Dilithium Zinc Silicate GammaII-Li_2ZnSiO_4. *Acta Crystallogr. Sect. B* **1979**, *35*, 2678–2680. [CrossRef]
65. Lyness, C.; Delobel, B.; Armstrong, A.R.; Bruce, P.G. The lithium intercalation compound Li_2CoSiO_4 and its behaviour as a positive electrode for lithium batteries. *Chem. Commun.* **2007**, 4890–4892. [CrossRef]
66. Keffer, C.; Mighell, A.; Mauer, F.; Swanson, H.; Block, S. Crystal Structure of Twinned Low-Temperature Lithium Phosphate. *Inorg. Chem.* **1967**, *6*, 119–125. [CrossRef]
67. Kieu My, B.; Van An, D.; Takahisa, O. Hybrid functional study on diffusion of silicate cathode material Li_2NiSiO_4. *J. Phys. Conf. Ser.* **2013**, *454*, 012061.
68. Ashcroft, N.W.; Mermin, N.D. *Solid State Physics*; Holt, Rinehart and Winston: New York, NY, USA, 1976.
69. Nye, J.F. *Physical Properties of Crystals*; Oxford University Press: Oxford, UK, 1985.
70. Watt, J.P. Hashin-Shtrikman bounds on the effective elastic moduli of polycrystals with orthorhombic symmetry. *J. Appl. Phys.* **1980**, *51*, 1520. [CrossRef]
71. Haines, J.; Leger, J.; Bocquillon, G. Synthesis and Design of Superhard Materials. *Annu. Rev. Mater. Res.* **2001**, *31*, 1–23. [CrossRef]
72. Anderson, O.L. A simplified method for calculating the debye temperature from elastic constants. *J. Phys. Chem. Solids* **1963**, *24*, 909–917. [CrossRef]
73. Pugh, S.F. Relations between the elastic moduli and the plastic properties of polycrystalline pure metals. *Lond. Edinb. Dublin Philos. Mag. J. Sci.* **1954**, *45*, 823–843. [CrossRef]
74. Deyirmenjian, V.B.; Heine, V.; Payne, M.C.; Milman, V.; Lynden-Bell, R.M.; Finnis, M.W. Ab Initio Atomistic Simulation of the Strength of Defective Aluminum and Tests of Empirical Force Models. *Phys. Rev. B* **1995**, *52*, 15191–15207. [CrossRef]

75. Marlo, M.; Milman, V. Density-functional study of bulk and surface properties of titanium nitride using different exchange-correlation functionals. *Phys. Rev. B* **2000**, *62*, 2899–2907. [CrossRef]
76. Milman, V.; Warren, M.C. Elastic properties of TiB_2 and MgB_2. *J. Phys. Condens. Matter* **2001**, *13*, 5585–5595. [CrossRef]
77. Ravindran, P.; Vajeeston, P.; Vidya, R.; Kjekshus, A.; Fjellvåg, H. Detailed electronic structure studies on superconducting MgB_2 and related compounds. *Phys. Rev. B* **2001**, *64*, 224509. [CrossRef]
78. de, A.; Manassidis, I.; Lin, J.S.; Gillan, M.J. The energetics of Frenkel defects in Li_2O from 1st principles. *Europhys. Lett.* **1992**, *19*, 605–610. [CrossRef]
79. Ravindran, P.; Fast, L.; Korzhavyi, P.A.; Johansson, B.; Wills, J.; Eriksson, O. Density functional theory for calculation of elastic properties of orthorhombic crystals: Application to $TiSi_2$. *J. Appl. Phys.* **1998**, *84*, 4891–4904. [CrossRef]
80. Karki, B.B.; Clark, S.J.; Warren, M.C.; Hsueh, H.C.; Ackland, G.J.; Crain, J. Ab initio elasticity and lattice dynamics of $AgGaSe_2$. *J. Phys. Condens. Matter* **1997**, *9*, 375–380. [CrossRef]
81. Reuss, A. Berechnung der Fließgrenze von Mischkristallen auf Grund der Plastizitätsbedingung für Einkristalle. *ZAMM* **1929**, *9*, 49–58. [CrossRef]
82. Hill, R. The Elastic Behaviour of a Crystalline Aggregate. *Proc. Phys. Soc. A* **1952**, *65*, 350. [CrossRef]
83. Voigt, W. *Lehrbuch der Kristallphysik*; B.G. Teubner: Leipzig, Germany, 1928.
84. Horn, R.A.; Johnson, C.R. *Matrix Analysis*; Cambridge University Press: Cambridge, UK, 2012; p. 664.
85. Luo, S.H.; Wang, M.; Sun, W.N. Fabricated and improved electrochemical properties of Li_2MnSiO_4 cathodes by hydrothermal reaction for Li-ion batteries. *Ceram. Int.* **2012**, *38*, 4325–4329. [CrossRef]
86. Vajeeston, Ionic conductivity enhancement by particle size reduction in Li_2FeSiO_4. *Mater. Lett.* **2018**, *218*, 313–316. [CrossRef]